GFZ

Helmholtz-Zentrum
POTSDAM

Assessing the Potential of Sun-Induced Fluorescence and the Canopy Scattering Coefficient to Track Large-Scale Vegetation Dynamics in Amazon Forests

Philipp Köhler[1,2], Luis Guanter[1], Hideki Kobayashi[3], Sophia Walther[1], and Wei Yang[4]

[1] *German Research Center for Geosciences (GFZ), Remote Sensing Section, Potsdam, Germany.*
[2] *California Institute of Technology (Caltech), Division of Geological and Planetary Sciences, Pasadena, CA, USA.*
[3] *Japan Agency for Marine-Earth Science and Technology (JAMSTEC), Department of Environmental Geochemical Cycle Research, Yokosuka, Japan.*
[4] *Center for Environmental Remote Sensing, Chiba University, Chiba, 263-8522, Japan.*

Abstract

Two new remote sensing vegetation parameters derived from spaceborne spectrometers and simulated with a three dimensional radiative transfer model have been evaluated in terms of their prospects and drawbacks for the monitoring of dense vegetation canopies: (i) sun-induced chlorophyll fluorescence (SIF), a unique signal emitted by photosynthetically active vegetation and (ii) the canopy scattering coefficient (CSC), a vegetation parameter derived along with the directional area scattering factor (DASF) and expected to be particularly sensitive to leaf optical properties. Here, we present the first global data set of DASF/CSC and examine the potential of CSC and SIF for providing complementary information on the controversially discussed vegetation seasonality in Amazon forests. A comparison between near-infrared SIF derived from the Global Ozone Monitoring Experiment-2 (GOME-2) instrument and the Orbiting Carbon Observatory-2 (OCO-2) (overpass time in the morning and noon, respectively) reveals the response of SIF to instantaneous photosynthetically active radiation (PAR). Large-scale seasonal swings of GOME-2 SIF amount up to 21% (regarding the annual maximum) and peak in October and around February, while OCO-2 SIF peaks in February. However, both time series agree very well if SIF is normalized by overpass time and wavelength. We further examine anistropic reflectance characteristics with the finding that the hot spot effect significantly impacts observed GOME-2 SIF values. On the contrary, our sensitivity analysis suggests that CSC is highly independent of sun-sensor geometry as well as atmospheric effects. The slight annual variability of CSC (3%) shows no clear seaonal cycle, while a relatively high spatial standard deviation points to a high degree of spatial heterogeneity in our study domain within the central Amazon Basin.

Keywords: *GOME-2, OCO-2, sun-induced chlorophyll fluorescence, concept of canopy spectral invariants, canopy scattering coefficient, directional area scattering factor, Amazon forest dynamics*

1 Introduction

The importance of the Amazon rainforest regarding its role in the global carbon cycle (e.g., Tian et al., 2000) and its species diversity (e.g., Ter Steege et al., 2013) is represented by a tremendous number of studies. Simultaneously, these studies also reveal the challenge posed by the complex ecosystem. Poorly accessible areas and the large extent of the Amazon Basin constrain ground-based observation capacities. Satellite-based remote sensing provides a crucial opportunity to continually monitor these areas, but even recent findings of satellite-based analyses addressing vegetation dynamics, seasonality, and responses to drought events remain contradictory.

The majority of studies report an increase ('green-up') in photosynthetic activity during months with less intense precipitation (usually June-October; e.g., Huete et al., 2006; Samanta et al., 2012; Bi et al., 2015). In contrast, Morton et al. (2014) claim that structure and greenness and thus photosynthetic activity remain constant if the satellite data is accurately corrected for directional reflectance effects in the measurement. These controversial results might be explained due to the fact that the monitoring of dense vegetation represents a complicated case in optical remote sensing. Reflected solar radiation saturates and becomes weakly sensitive to vegetation changes, and there is a substantial influence of changing sun-sensor geometry and residual atmospheric effects (Verrelst et al., 2008; Hilker et al., 2015; Maeda and Galvão, 2015).

Thanks to recent advances in the analysis of spaceborne spectroscopic measurements two new and promising vegetation parameters have become available - sun-induced chlorophyll fluorescence (SIF) and the canopy scattering coefficient (CSC). While SIF is directly related to photosynthesis, CSC is a structural parameter assumed to be particularly sensitive to leaf properties (Samanta et al., 2012; Knyazikhin et al., 2013). Considering that Roberts et al. (1998) observed a 10% increase in the near-infrared (NIR) absorption in matured tropical leaf spectra, the CSC may capture leaf age-effects. A strong argument to lay particular emphasis on such effects was recently raised by Wu et al. (2016). They specifically examined seasonal variations of several vegetation parameters from ground, tower, and satellite measurements at four sites in the Amazon and concluded that the canopy phenology, i.e. the leaf age, drives the photosynthetic seasonality rather than seasonal variations of climate conditions. It would clearly be beneficial if a basin-wide measure of leaf phenology could be established. Three characteristics of SIF might be advantageous compared to traditional reflectance-based vegetation indices (VIs): (i) a saturation of SIF has not yet been observed, (ii) SIF appears to be less affected by sub-pixel clouds (Frankenberg et al., 2012; Guanter et al., 2015), (iii) SIF is expected to provide a direct link to actual photosynthetic rates, while greenness based indices indicate potential photosynthesis represented by their response to chlorophyll content. Both SIF and CSC may therefore contain relevant information to re-assess vegetation dynamics in the Amazon region.

Global SIF data sets are available from several spaceborne sensors, including:

(i) Greenhouse Gases Observing Satellite-Fourier Transform Spectrometer (GOSAT-FTS; Frankenberg et al., 2011a; Joiner et al., 2011, 2012; Guanter et al., 2012; Köhler et al., 2015a),

(ii) SCanning Imaging Absorption SpectroMeter for Atmospheric CHartographY (SCIAMACHY; Joiner et al., 2012; Köhler et al., 2015b; Wolanin et al., 2015),

(iii) Global Ozone Monitoring Experiment-2 (GOME-2; Joiner et al., 2013; Köhler et al., 2015b; Wolanin et al., 2015),

(iv) Orbiting Carbon Observatory-2 (OCO-2; Frankenberg et al., 2014).

However, only a few studies relating SIF to productivity in tropical forests can be found in published research so far. Lee et al. (2013) and Parazoo et al. (2013) reported that wet season productivity (estimated using SIF) exceeds the 'dry' season productivity in southern Amazon forest regions where pronounced precipitation variations occur. Guan et al. (2015) examined global tropical evergreen forest regions and concluded that the photosynthetic activity can be

maintained during the drier season if the annual water availability is sufficient.

Based on the concept of canopy spectral invariants (e.g., Knyazikhin et al., 2011), Samanta et al. (2012) expressed the spectral reflectance in terms of directional area scattering factor (DASF; Knyazikhin et al., 2013) and CSC (Smolander and Stenberg, 2005). By means of detailed theoretical considerations with respect to this expression, Samanta et al. (2012) argues that changes in NIR reflectance of Amazon forests could be explained by both changes in leaf area and leaf optical properties, but unlikely by changes in leaf area alone. Leaf optical property variations due to leaf aging effects translate into changes in CSC. However, Samanta et al. (2012) simultaneously acknowledges that leaf optical variations might also be caused by coating substances like water or dust.

GOME-2 is at present the only spaceborne spectrometer that provides time series of spectroscopic measurements in the 650–800 nm wavelength range, enabling simultaneous computations of DASF, CSC, SIF, and NDVI. An encouraging aspect for retrieving several vegetation parameters from GOME-2 data lies in the wide range of covered observation geometries, allowing to address directional effects. While the importance of directional effects has increasingly been recognized when analyzing VIs, less is known about the effects on satellite-based SIF data sets. However, several studies suggest considering changing illumination and view conditions (van der Tol et al., 2009; Guanter et al., 2012; Damm et al., 2015; Liu et al., 2016). Another benefit of simultaneous retrievals of different vegetation parameters from a single sensor is the consistent spatial sampling, even though GOME-2 measurements have a relatively coarse spatial resolution as opposed to the more frequently used products obtained from the Moderate Resolution Imaging Spectroradiometer (MODIS). The large footprint size of GOME-2 (40 km x 40 km) likely involves undetected sub-pixel clouds, which indicates a further limiting factor.

We primarily aim to evaluate prospects and drawbacks of both SIF and CSC for tracking vegetation dynamics and productivity in Amazon forests by examining simulated and real satellite data. We present SIF time series derived from measurements of the GOME-2 instrument (Köhler et al., 2015b) and from OCO-2 (Frankenberg et al., 2014) for a region within the central Amazon Basin and subsequently discuss limitations due to sun-sensor geometry and illumination conditions at the overpass time. DASF and CSC have been computed from atmospherically corrected GOME-2 data, which enables us to present the first global data set of these parameters. We have also computed the well-established Normalized Difference Vegetation Index (NDVI) and made use of supplementary data sets to provide a basis for interpreting the obtained results. Finally, we present long-term monthly averages to illustrate the large-scale seasonality of SIF, CSC, and NDVI in the Amazon forest, as seen from the GOME-2 instrument.

2 Data & Methods

2.1 GOME-2

We use spectral radiance measurements from the GOME-2 instrument onboard EUMET-SAT's polar orbiting Meteorological Operational Satellite MetOp-A (Munro et al., 2006) acquired between August 2013 and August 2016. This time period has been selected because the swath width has changed since July 15th, 2013 from 1920 km to 960 km, resulting in a reduced ground pixel size of about 40 km x 40 km (previously 80 km x 40 km). Spectra acquired by the fourth detector channel, covering the 600 to 790 nm spectral range with a resolution of 0.5 nm and a signal-to-noise ratio up to 2000, are relevant for our analysis. The effective cloud fraction from the Fast Retrieval Scheme for Clouds from the O2 A-band (FRESCO, Wang et al., 2008) was used for cloud screening.

2.2 Study Domain & Spatial Averaging

Our analysis of large-scale vegetation dynamics (Sect. 4.4) is focused on a domain in southern Amazonia, indicated by the red box in Fig. 1 (latitudes between 0° - 10° S and longitudes between 70°W–50°W). Special care has been taken to minimize the impact of structural composition effects on the resulting time
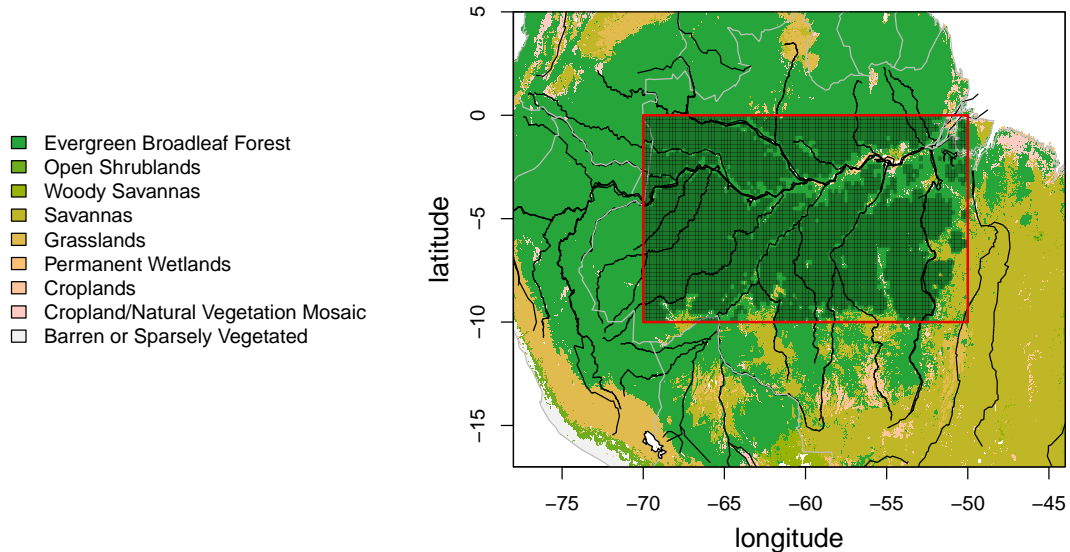
Figure 1: IGBP land classification (Friedl et al., 2002). The darkened areas within the red box define the study domain.

series.

At first, GOME-2 measurements are pre-selected based on the International Geosphere and Biosphere Program (IGBP) land classification (Friedl et al., 2002) shown in Fig. 1. The main land cover is determined under consideration that each GOME-2 footprint has a spatial extent represented by a polygon. Measurement polygons, classified as evergreen broadleaf forest with a land cover fraction higher than 0.9, formed the basis for the spatial average. Pre-selected polygons were subsequently averaged on a monthly basis on a 0.2° x 0.2° grid (about 22 km x 22 km), while a value contributes to the grid cell average if the polygon covers the center of a grid cell. The study domain is further confined by masking grid cells, which potentially own differing structural properties when compared to the majority of grid cells. In particular, a k-means approach has been applied to the supplementary leaf area index (LAI) data set (see Sect. 2.8) to identify such grid cells. The remaining grid cells, shown as darkened areas in Fig. 1, define the underlying region for the actual analysis. It is remarkable that particularly grid cells close to the Amazon River and other water bodies were identified to have different structural properties, which might be associated with large floodplain areas (Várzea forests).

2.3 Sun-Induced Chlorophyll Fluorescence (SIF)

Chlorophyll pigments in terrestrial vegetation absorb sunlight to cover the energy demand during the process of photosynthesis. A part of the excess energy dissipates as sun-induced fluorescence (SIF) emitted by chlorophyll a in the red and NIR spectral region (650-800 nm). Though the amount of SIF represents only a few percent of the total light energy absorbed, SIF measurements can serve as a valuable tool to assess the photosynthetic performance of vegetation. In this context, it is important to consider the instantaneous nature of satellite-based SIF data when evaluating seasonal cycles. For example, SIF intrinsically depends on the illumination condition at the overpass time, while temporal trajectories of illumination at certain daytimes can result in different seasonalities (i.e. shifted annual maximum/minimum, discussed in detail in Sect. 4.2). Here, we analyze SIF estimates from GOME-2 (overpass time at ∼9:30 local solar time, LST) and OCO-2 (overpass time at ∼13:30 LST) data derived with fundamentally different retrieval approaches as discussed below.

2.3.1 GOME-2 SIF

The retrieval methodology of the GOME-2 SIF data set used in this study was described by Köhler et al. (2015b). This data set has been extended until August 2016 (previously 2007-2011) and can be retrieved from `ftp://ftp.gfz-potsdam.de/home/mefe/GlobFluo/`. GOME-2 SIF retrievals generally rely on a statistically based approach to separate the SIF emission from spectral features related to atmospheric absorption, scattering, and surface reflectance. This specific retrieval essentially reconstructs the radiance spectrum in the 720-758 nm interval and provides a value for the second of two characteristic peaks of the fluorescence emission spectrum at 740 nm. Modeled spectra are compared to the original measurements to exclude corrupted retrievals. This is done by a radiance residual check, which has been reinforced for our investigation in the Amazon Basin to reduce the impact of potential error sources on resulting time series. Joiner et al. (2013) and Köhler et al. (2015b) reported that the South Atlantic Anomaly, a region with an anomalously reduced strength in the Earth's magnetic field, leads to an increased retrieval noise in large parts of the South American continent. Therefore, we limited the residual sum of squares (RSS) to 0.5 (mW m^{-2} sr^{-1} nm^{-1})^2 instead of using the 2 (mW m^{-2} sr^{-1} nm^{-1})^2 threshold documented by Köhler et al. (2015b). The number of evaluated retrievals within the study domain is consequently reduced by about two thirds.

2.3.2 OCO-2 SIF

The OCO-2 instrument was launched in July 2014 and provides spectrally high resolved measurements in the O$_2$ A-band (757-775 nm, FWHM=0.042 nm), which allows to evaluate the in-filling of solar Fraunhofer lines at 757 and 770.1 nm by SIF (Frankenberg et al., 2014). OCO-2 acquires 24 spectra per second with a much smaller ground-pixel size (1.3 km x 2.25 km) as compared to GOME-2 (40 km x 40 km). The high spectral resolution enables robust and accurate retrieval results (Frankenberg et al., 2014), but the fine spatial sampling with the narrow swath width of 10.3 km increases the revisit time up to 16 days (GOME-2: 3 days) and involves a lack of continuous global coverage (i.e. gaps between swaths for a full repeat cycle). Here, we use cloud free nadir observations of offset corrected OCO-2 SIF (version B7101) between September 2014 and August 2016. We average both OCO-2 SIF retrieval results (valid at 757 and 770.1 nm, respectively) after multiplying SIF at 770.1 with 1.7, as documented in the OCO-2 Data Product User's Guide (Version F, page 33).

2.3.3 SIF normalization

In order to facilitate an inter-sensor/retrieval comparison, the influence of instantaneous illumination conditions has to be removed and a wavelength correction has to be applied. A common approach is to normalize the retrieved SIF value by the cosine of the solar zenith angle (e.g., Joiner et al., 2013). This approach is assumed to extract a possible underlying seasonality (besides the instantaneous PAR driven seasonality), but might only be applicable in areas where SIF is relatively high throughout the year. Noise in SIF would otherwise be amplified, especially for low SIF values in combination with inclined illumination angles. Furthermore, second order characteristics such as the amount of sunlit/shaded leaves are likely to become more pronounced.

Another normalization method was proposed by Frankenberg et al. (2011b), taking into account variations in overpass time, length of day, and solar zenith angle. In particular, this approach provides a first order approximation for a daily SIF average

$$\hat{SIF} = SIF/cos(\theta_0(t_m)) \cdot \int_{t=t_m-12h}^{t=t_m+12h} cos(\theta_0(t)) \ dt, \quad (1)$$

where θ_0 is the solar zenith angle and t_m is the measurement time. The normalization is applied to individual GOME-2 soundings by computing the numerical integral in 10 minute time-steps (dt), which is consistent with correction factors provided in the OCO-2 data set. The SIF value at 740 nm (second characteristic peak) is typically assumed to be about 1.5 times higher than SIF at 757 nm (e.g., Joiner

5

et al., 2013). The 1.5 conversion factor is consistent with leaf-level studies on passive SIF across a wide range of species and individuals using the instrumentation described in Magney et al. (2017). We, therefore, multiply OCO-2 SIF by this factor to account for the difference in evaluated wavelengths in addition to the daily correction when we directly compare both data sets in Sect. 4.2.

2.4 Atmospheric Correction of GOME-2 Radiance Spectra

Radiance received by GOME-2 at the top-of-atmosphere (TOA) is composed of direct and diffuse irradiance contributions from both atmosphere and surface. The magnitude of atmospheric effects can vary largely depending on the atmospheric state, surface properties and wavelength. Thus, it is necessary to correct the TOA signal for atmospheric effects to estimate the actual surface reflectance (ρ_s), which is in turn used to derive other parameters (ρ_{NIR}, DASF, CSC, and NDVI).

We based the atmospheric correction on simulations performed with the Matrix Operator MOdel (MOMO) radiative transer code (Fell and Fischer, 2001), mostly consistent to a subset of simulations used in Joiner et al. (2013); Guanter et al. (2015); Köhler et al. (2015b). Simulations were performed between 500 nm and 800 nm with a spectral sampling of 0.005 nm and included three viewing zenith angles (0°, 16°, 27°), four solar zenith angles (15°, 30°, 45°, 70°), a mid-latitude summer temperature profile, four surface pressures (955, 980, 1005, 1030 hPa), four water vapour columns (0.5, 1.5, 2.5, 4.0 g cm^{-2}), an aerosol layer height between 600–800 hPa using a continental aerosol model, and five aerosol optical thicknesses at 550 nm (0.05, 0.12, 0.2, 0.3, 0.4).

A solution for the radiative transfer in a plane-parallel atmosphere with a perfectly diffuse (Lambertian) surface can be formulated as

$$F_{TOA} = F_0 + \frac{E_g \cdot \rho_s}{\pi(1 - \rho_s S_{atm})}, \qquad (2)$$

where F_{TOA} is the (measured) TOA radiance, F_0 is the atmospheric path radiance, E_g is the transmitted global irradiance (direct and diffuse), S_{atm} is the atmospheric spherical albedo (i.e. the reflectance of the atmosphere for

isotropic light entering it from the surface), and ρ_s is the surface reflectance (all variables own a spectral component). F_{TOA}, F_0, E_g, and S are assumed to be functions of solar zenith angle (SZA), viewing zenith angle (VZA), mean sea level pressure (MSL), water vapour column (WVC), and aerosol optical thickness at 550 nm (AOD). Azimuthal resolution of sun-sensor geometry and adjacency effect are not included. Although a natural surface reflects solar radiation anisotropically, we assume that Lambertian equivalent surface reflectance estimates through Eq. (2) satisfy the requirements for this analysis. Hu et al. (1999) evaluated relative errors in canopy reflectance estimates for MODIS data when using a Lambertian assumption. They reported that MODIS relative errors are about 5% in the red band and 2% in the NIR band (for hardwood forest and an AOD of 0.2; median AOD of observations used here is about 0.15).
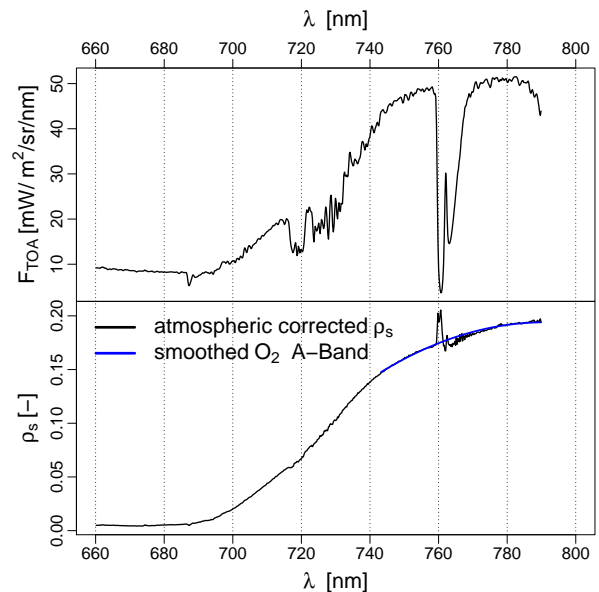

Figure 2: Sample measurement spectrum of GOME-2 and atmospherically corrected surface reflectance estimate between 660-790 nm (633 spectral points). The measurement within the study domain (center latitude 1.1° S, center longitude 57.3° W) was carried out at 07/04/2014, atmospheric correction was performed with following input parameters: SZA = 46.8°, VZA = 10.7°, AOD = 0.06, WVC = 3.87 g/cm^2, MSL = 1015.4 hPa. A second order polynomial fit using the 743-758 mn and 774-782 nm spectral intervals (blue) is applied to replace the unreasonable reflectance estimates inside the O$_2$ A-band (759-774 nm) by fitted values.

A lookup table approach in conjunction with supplementary data sets (see Sect. 2.8) of MSL, WVC, and AOD is applied to estimate the

spectral bidirectional reflectance. Fig. 2 depicts a sample measurement spectrum of GOME-2 together with the atmospherically corrected surface reflectance estimate in the relevant wavelength range between 660–790 nm. It needs to be mentioned that the highly complex radiative transfer in the strong absorption O_2 A-band (759-774 nm) causes a high frequency spectral pattern in ρ_s, although vegetation has a spectrally smooth reflectance signature in the considered wavelength range. We therefore fitted a second order polynomial to the reflectance in two spectral windows around the O_2 A-band, assumed to be mostly devoid of atmospheric absorption (743-758 mn and 774-782 nm), and replaced the unreasonable reflectance estimates.

2.5 Directional Area Scattering Factor (DASF) & Canopy Scattering Coefficient (CSC)

We adopted the approach of Knyazikhin et al. (2013) to retrieve CSC from atmospherically corrected NIR reflectances using GOME-2 data. This approach relies on the idea to scale scattering processes from the leaf to the canopy level. The theory of such a scaling has made significant progress since one of the initial attempts from Knyazikhin et al. (1998). In particular, the concept of canopy spectral invariants (summarized in Huang et al., 2007) provides the basis for a physically consistent, and thus more direct, approach to relate reflectance-based measurements to leaf structure and biochemistry.

It should be mentioned that the recollision probability (p) for scattered photons within a canopy is wavelength independent (spectral invariant), because scattering objects are large compared to the wavelengths of solar radiation (Lewis and Disney, 2007). Smolander and Stenberg (2005) have shown that a combination of different recollision probabilities on the leaf level, namely for shoots and needles as the most important scattering elements within coniferous canopies, results in one equivalent recollision probability on the canopy scale. When neglecting leaf surface reflection (Lewis and Disney, 2007), the scaling even applies from the leaf interior to the canopy level. Besides simulation based studies (Knyazikhin et al.,

1998; Smolander and Stenberg, 2005; Huang et al., 2007; Lewis and Disney, 2007), the p theory has been succesfully applied to remote sensing applications (e.g, Schull et al., 2011; Knyazikhin et al., 2013). Particularly the study from Knyazikhin et al. (2013) may have long-term consequences for the remote sensing assessments of biochemistry. They introduced the following representation of the canopy bidirectional reflectance (BRF)

$$BRF_\lambda(\Omega) = DASF(\Omega) \cdot W_\lambda, \qquad (3)$$

where Ω is the direction towards the sensor, DASF is the directional area scattering factor and W_λ the (wavelength dependent) canopy scattering coefficient. It might be noted that BRF_λ is equivalent to ρ_s in Eq. (2). The wording is changed in this section to remain consistent with the literature. Furthermore, it should be emphasized that W_λ refers to the spectral canopy scattering coefficient, while the abbreviation CSC refers to the canopy scattering coefficient at NIR wavelengths (discussed below in Sect. 2.5.2). The DASF is a spectral invariant estimate of the BRF_λ for a non-absorbing canopy and encapsulates canopy structure properties such as the tree spatial distribution. The key benefit of the approach from Knyazikhin et al. (2013) is that no prior knowledge is needed to estimate the DASF from reflectance spectra in the 710 to 790 nm spectral interval.

2.5.1 DASF Estimation

Assuming that the observed canopy is sufficiently dense (background/surface effects are negligible), the spectral bidirectional reflectance (BRF) can be approximated as (Knyazikhin et al., 2011)

$$BRF_\lambda(\Omega) = \frac{\rho(\Omega)i_0(\Omega_0)\omega_\lambda}{1 - \omega_\lambda p}, \qquad (4)$$

where $\rho(\Omega)$ is the directional gap density giving the escape probability for scattered photons in direction Ω, $i_0(\Omega_0)$ is the initial collision probability or canopy interceptance for the direction of incoming radiation Ω_0 (fraction of photons that initially collide with foliage elements, close to unity in dense vegetation canopies), p is the mean probability that a scattered photon

will interact within the canopy again (recollision probability) and ω_λ is the canopy albedo.

Eq. (4) is still formulated on the canopy level, but p implicitly incorporates the scaling to the leaf level. Specifically, the scaling to the next smaller structural organization (i.e. from the canopy to the leaf level) can be expressed by accumulated scattering orders of local recollision probabilities (Smolander and Stenberg, 2005)

$$\omega_\lambda = \sum_{n=0}^{\infty} [p_L^n \omega_{L,\lambda}^n (1 - p_L)] =$$
$$\frac{1 - p_L}{1 - p_L \omega_{L,\lambda}} \omega_{L,\lambda}, \quad (5)$$

where the leaf scale is indicated by the subscripted L. Specifically, p_L characterizes the probability of photons being scattered inside the leaf and $\omega_{L,\lambda}$ is the leaf-level single scattering albedo. An empirical analysis of measured leaf albedo spectra suggests that one fixed reference leaf albedo ($\omega_{0,\lambda}$) can be used instead of the actual single leaf albedo ($\omega_{L,\lambda}$) without violating the spectral invariant relationship from Eq. (5) in the 710 to 790 nm spectral interval (Schull et al., 2011). It is further necessary to decompose ω_λ into

$$\omega_\lambda = i_L \bar{\omega}_\lambda + s_L, \quad (6)$$

where i_L is the leaf interceptance, $\bar{\omega}_\lambda$ is the transformed leaf albedo giving the fraction of photons scattered by the interior of leaves and s_L is the portion of photons reflected from the leaf surface. Assuming that the scattering by the leaf interior dominates in the 710 to 790 nm spectral region, Eq. (5) becomes (Knyazikhin et al., 2013)

$$\omega_\lambda \approx i_L \bar{\omega}_\lambda = \frac{1 - p_L}{1 - p_L \omega_{0,\lambda}} i_L \omega_{0,\lambda}, \quad (7)$$

where $\omega_{0,\lambda}$ is the fixed reference leaf albedo, which has been derived with the PROSPECT model (chlorophyll content of 16 μg cm^{-2}, equivalent water thickness of 0.005 cm^{-1}, dry matter content of 0.002 g cm^{-2} as suggested by Knyazikhin et al., 2013). By substituting Eq. (7) into Eq. (4) and rearranging terms, Knyazikhin et al. (2013) arrived at

$$\frac{BRF_\lambda(\Omega)}{\omega_{0,\lambda}} = p_{eff} BRF_\lambda(\Omega) +$$
$$i_L \rho(\Omega) i_0(\Omega_0)(1 - p_L), \quad (8)$$

with $p_{eff} = p_L + i_L p(1 - p_L)$. p_{eff} is equivalent to the spectral invariant relationship between recollision probabilities of shoots and needles documented by Smolander and Stenberg (2005). Here, p_{eff} describes the scattering within leaves as seen from the canopy level, i.e. the probability of being scattered inside the leaf (p_L) is combined with the probability that a photon escapes the leaf ($1 - p_L$) and enters another leaf within the canopy ($i_L p$). A simple linear regression between $BRF_\lambda/\omega_{0,\lambda}$ vs. BRF_λ (see Eq. 8) gives the slope $m = p_{eff}$ and intercept $n = i_L \rho(\Omega) i_0 (1 - p_L)$. Finally, the ratio $n/(1 - m)$ results in the following representation of the DASF (Knyazikhin et al., 2013)

$$DASF(\Omega) = \frac{i_L \rho(\Omega) i_0(\Omega_0)}{1 - i_L p}. \quad (9)$$

DASF becomes independent of p_L; moreover, the DASF appears to be independent of the choice of $\omega_{0,\lambda}$ (Schull et al., 2011), which both seem reasonable considering that the DASF conveys macro-structural properties. The R^2 value of the linear fit in the 710-790 nm spectral region indicates the retrieval quality and applicability of assumptions (e.g., sufficiently dense vegetation). Our analysis is therefore based on DASF retrievals with a R^2 value above 0.9 (this threshold will be further discussed in Sect. 4.1). It is further worth noting that NIR reflectance and DASF are closely related in terms of their sensitivity to view-illumination conditions.

2.5.2 CSC Estimation

When expressing BRF_λ in terms of DASF and W_λ (Eq. 3), and considering that the DASF conveys macro-structural properties, leaf properties (represented by W_λ) can potentially be extracted from reflectance measurements through the ratio $BRF_\lambda/DASF$. In contrast to visible wavelengths, where pigment absorption dominates, residual variations in the NIR are mostly due to canopy/leaf structure (Hikosaka et al., 2015). Here, the 780-785 nm NIR spectral interval serves as weakly absorbing wavelength range to compute CSC (or W_{NIR}).

An analytical representation of W_λ is given by (Knyazikhin et al., 2013)

$$W_\lambda = \frac{1 - p i_L}{1 - \hat{\omega}_\lambda p i_L} \hat{\omega}_\lambda, \quad (10)$$

8

with $\hat{\omega}_\lambda = \omega_\lambda / i_L$. In this case, p is the probability that a scattered photon will interact again within the canopy (recollision probability), ω_λ is the leaf albedo and i_L is the leaf interceptance (fraction of radiation that enters the leaf interior). Note that Eq. (10) includes no explicit dependency on illumination or observation geometry, although the leaf albedo is in principle subject to a certain bidirectional reflectance distribution function (BRDF). However, considering that the ground pixel size of GOME-2 (40 km x 40 km) involves a vast number of leaves, it can be anticipated that any angular preference will tend to average out. Conceptually, this vegetation parameter should therefore be independent of sun-sensor geometry, which is supported by our results in Fig. 9 of Sect. 4.3.

W_λ increases as the albedo increases, but as can be seen from Eq. (10), W_λ is also subject to changes in canopy structure through the dependency on the p value. More specifically, p increases with LAI (Knyazikhin et al., 1998; Smolander and Stenberg, 2005), which can be explained by a higher chance for photons to be absorbed (Samanta et al., 2012). Consequently, the absolute value of W_λ decreases with increasing LAI, which potentially complicates the interpretation of time series to account for actual leaf properties. We will evaluate this sensitivity based on simulated data in Sect. 3.2.

The formalism to compute DASF and CSC can be summarized as follows:

1. Perform atmospheric correction of measured BRF_λ (Sect. 2.4).

2. Perform a linear fit between $BRF_\lambda / \omega_{0,\lambda}$ vs. BRF_λ in the 710–790 nm spectral window (389 spectral points), where $\omega_{0,\lambda}$ is a reference leaf albedo (Sect. 2.5.1).

3. The ratio $n/(1-m)$ of slope, m, and intercept, n, from the linear fit results in DASF as represented by Eq. (9).

4. CSC (W_{NIR}) results from the ratio $BRF_{NIR}/DASF$, where BRF_{NIR} is the averaged atmospherically corrected reflectance between 780-785 nm.

It must be noted that the approach of Knyazikhin et al. (2013) considers green foliage elements only, even though photons interact with the whole canopy (green, non-green, or woody foliage elements). This is a further limitation of our study, which may result in inaccurate estimates of DASF/CSC in terms of absolute values. However, in the framework of this analysis we consider seasonal changes to be more important than accurate absolute values. We assume that the portion of green foliage elements dominates and that there are only minor temporal changes in the ratio between green/brown material in the canopy at the spatial scale under investigation.

2.6 Normalized Difference Vegetation Index

For the sake of comparison, the simple but effective Normalized Difference Vegetation Index (NDVI, Tucker, 1979) has been computed from GOME-2 data. The standard definition is given by the band ratio

$$NDVI = \frac{\rho_{NIR} - \rho_{RED}}{\rho_{NIR} + \rho_{RED}}, \qquad (11)$$

where ρ_{NIR} and ρ_{RED} are computed from averaged atmospherically corrected reflectances between 780-785 nm and 660-665 nm. Joiner et al. (2013) reported that GOME-2 NDVI spatial patterns are similar to those of the MODIS NDVI product, even when atmospheric effects are not considered.

We acknowledge that the large-scale NDVI seasonality in the central Amazon Basin will potentially result from seasonal variations in cloud cover (Kobayashi and Dye, 2005; Hilker et al., 2015). Nevertheless, we believe that a spatially consistent comparison of GOME-2 SIF and CSC with a conventional VI provides an improved basis for interpretation.

2.7 Characterization of Sun-Sensor Geometry

Four angles are needed to characterize the illumination and observation geometry namely: solar zenith angle (θ_0), solar azimuth angle (ϕ_0), viewing zenith angle (θ_v), and viewing azimuth angle (ϕ_v). The position of the azimuth angles to each other can also be expressed by the relative azimuth angle (ϕ), where $\phi = 180°$ means that the sun and satellite sensor are oppositely aligned. It is further convenient to

combine θ_0, θ_v and ϕ to the phase angle (γ) by applying the spherical law of cosines

$$\gamma = acos[cos(\theta_0)cos(\theta_v)+ \\ sin(\theta_0)sin(\theta_v)cos(\phi)], \quad (12)$$

which gives the angle between the directions to the sun and detector as seen from the surface (Hapke, 2012). Here, γ is defined positive if the solar azimuth angle is larger than the viewing azimuth angle and negative otherwise, to be able to separate those cases. The phase angle replaces three angles to characterize the sun-sensor geometry, while approaching $\gamma = 0°$ corresponds to the situation when the sun and sensor are located along one axis.

Fig. 3 depicts the illumination and viewing conditions for GOME-2 measurements within our study domain. The seasonality of the sun-sensor geometry is comparable to MODIS observations shown by Bi et al. (2015). Several studies (Morton et al., 2014; Maeda and Galvão, 2015; Verrelst et al., 2008; Hilker et al., 2015) highlight the importance to take such a seasonality into account when evaluating VIs. In the case of MODIS, measurements are typically related to a fixed sun-surface-sensor geometry. We follow another strategy in Sect. 4.4; GOME-2 observations are limited to phase angles from $-65°$ to $-40°$, because this range of angles occurs in all considered months. This way, a seasonality in sun-sensor geometry and a potential influence on time series can be avoided.

2.8 Supplementary Data

A series of data is required for our atmospheric correction and for providing a basis to interpret the results obtained. The following list briefly summarizes all supplementary data sets used in this study.

a) Cloud free nadir observations of offset corrected OCO-2 SIF at 757 nm and 770.1 nm (Frankenberg et al., 2014, version B7101) between September 2014–August 2016.

b) IGBP land cover (Friedl et al., 2002) provided on a 0.05° x 0.05° (about 5 km x 5 km) grid.

c) LAI (Baret et al., 2013) from the Copernicus Global Land Service. Specifically, the SPOT-VGT LAI (version 1.3) is used between 08/2013 and 05/2014 and the PROBA-V LAI (version 1.4) from 06/2014 to 08/2016. Both data sets are provided on a 10-day basis with a spatial resolution of 1 km and have been aggregated to monthly averages on a 0.2° x 0.2° grid.

d) Collection 5 of the Aqua MODIS NDVI data provided on a 0.05° x 0.05° grid (MYD13C1, 2016, 16-day Vegetation Indices) quality flagged as good ('use with confidence'), aggregated to monthly averages on a 0.2° x 0.2° grid.

e) Monthly precipitation data from the Tropical Rainfall Measuring Mission (TRMM, 2011, product 3B43 version 7) on a 0.25° x 0.25° grid.

f) ERA-Interim re-analysis data (Dee et al., 2011) of photosynthetically active radiation (PAR, 400-700 nm, 3-hourly), WVC (6-hourly) and MSL (6-hourly). Here, WVC and MSL (PAR) data sets on a 0.75° x 0.75° (0.125° x 0.125°) grid have been used.

g) AOD (6-hourly) from the Monitoring Atmospheric Composition and Climate (MACC, 2016) re-analysis data set on a 0.75° x 0.75° grid.

2.9 Simulated SIF and Reflectance

Radiative transfer simulations of SIF and reflectance provide a possibility to review the basic validity of assumptions made. Furthermore, a discrepancy of observations with respect to the simulated data may point to specific characteristics and problems.

Simulations of incoming PAR, top of canopy (TOC) reflectance, and TOC SIF between 650 and 850 nm have been computed by the spatially explicit three dimensional plant canopy radiative transfer model (FLiES, Kobayashi and Iwabuchi, 2008), which is capable of simulating the multiple scattering within the plant canopy. We adopted the boundary conditions from the sun-sensor geometry of GOME-2 (Sect. 2.7) in combination with monthly averages of the LAI data set for 2014. Monthly av-
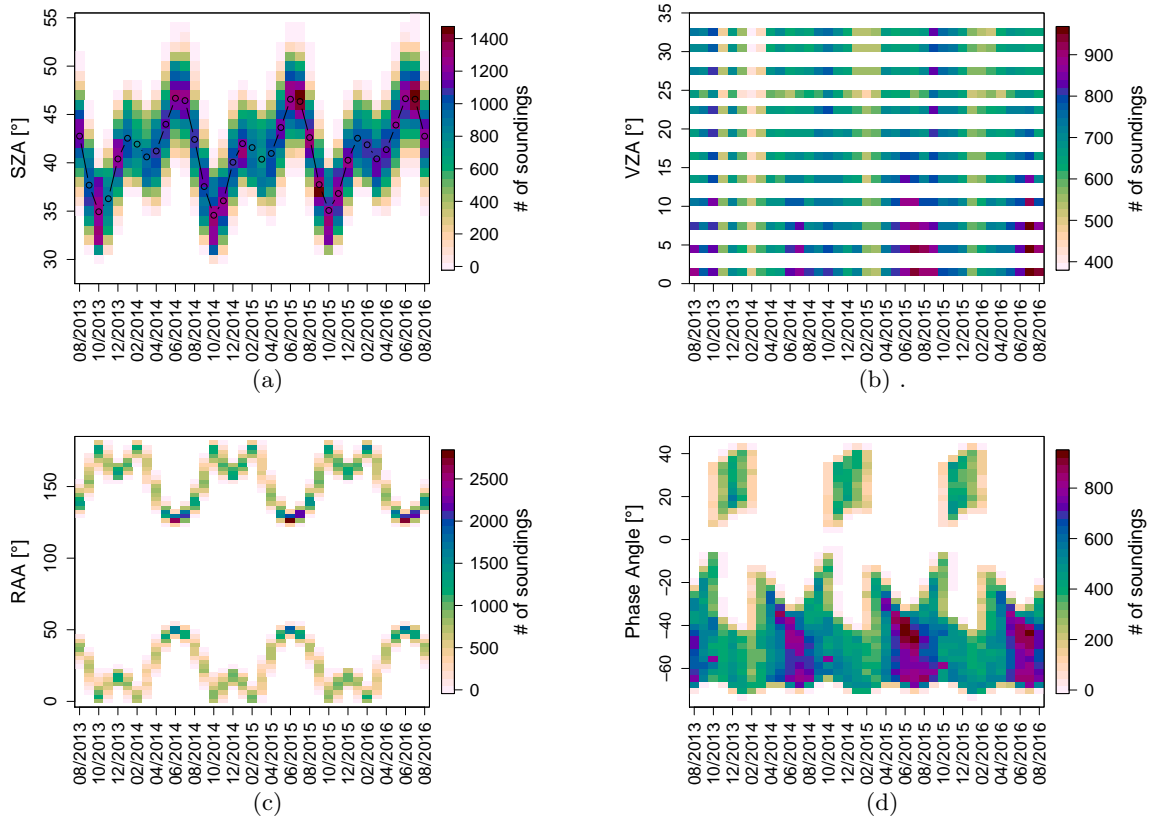
Figure 3: Viewing and illumination geometry of GOME-2 within our study domain. Shown are (a) solar zenith angle, (b) viewing zenith angle, (c) relative azimuth angle and (d) phase angle (Eq. 12).

erages of the solar zenith angle represent a simplified annual cycle of illumination, whereas all discrete viewing zenith angles as well as averages of the two separate regimes of the relative azimuth angle represent the observation geometry. The LAI ranges from 4.02 to 5.39 units, incorporating a changing canopy structure. Further, a realistic tropical forest landscape has been simulated by the empirical forest structure dynamics model (Yang et al., 2017). Detailed information about simulations of SIF and bidirectional reflectance can be found in A.

Figure 4: Simulated relative intensity changes of SIF, NDVI, rho_{NIR}, DASF and CSC as a function of cloud optical thickness (COT) for optically thin clouds.

3 Sensitivity Analysis

3.1 Sensitivity to Cloud Effects

Even though the impact of clouds on computed GOME-2 vegetation parameters can be limited by means of the FRESCO cloud fraction data attached to GOME-2 measurements, residual cloud contamination (i.e. undetected sub-pixel clouds) might be unavoidable due to the frequent cloud cover in tropical rainforest areas in combination with the large GOME-2 footprint
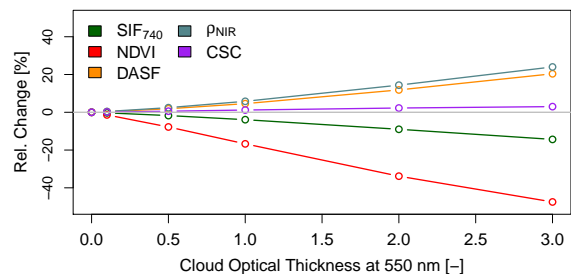
size. It is therefore crucial to examine potential cloud effects before a possible seasonality can be identified.

Here, simulated TOA radiance spectra as described in Sect. 2.4 have been used by incorporating different levels of cloud optical thickness (COT) values. Notably, the simulations are consistent with those used by Guanter et al. (2015).

Fig. 4 illustrates the sensitivity of SIF, NDVI, ρ_{NIR}, DASF and CSC to COT values

11

ranging from 0–3, corresponding to optically thin cirrus or scattered cumulus clouds. Surprisingly, CSC appears to be highly independent of atmospheric effects (+3% at a COT of 3), because the dependencies of DASF and ρ_{NIR} on cloud contamination tend to compensate by rationing. SIF appears to be only moderately affected by cloud contamination, which basically reflects previous findings of decreasing SIF values through the shielding effect by clouds (Frankenberg et al., 2012; Guanter et al., 2015). On the contrary, considerably decreasing NDVI values with an increasing COT may complicate the further evaluation. This strong effect can essentially be explained by the impact of clouds on both red and NIR wavelengths in addition to the shielding of the green vegetation.

Overall, it should be mentioned that the unknown degree of undetected cloud contamination of GOME-2 measurements represents the most limiting factor of this analysis.

3.2 Sensitivity of DASF & CSC to LAI

The question may arise, to which extent DASF and CSC are influenced by canopy structure (through the sensitivity of p to LAI) under the conditions in the Amazon rainforest. It is therefore essential that the simulations (Sect. 2.9) allow us to review this aspect.

The simulations include soil absorption and are driven with constant leaf properties, while LAI and sun-sensor geometry vary similarly to real GOME-2 observations. Given that DASF is an estimate for the non-absorbing canopy's reflectance, the DASF should be consistently higher than the NIR reflectance (ρ_{NIR}) to support the basic applicability of the p theory in our simulations. A similar seasonality of CSC and LAI would then indicate the expectable magnitude of a response of CSC to LAI.

The upper panel of Fig. 5 reveals that the DASF is indeed higher than ρ_{NIR}, which is consistent with the underlying theory. NIR reflectance/DASF intensity changes highly correlates with the LAI input values ($R = 0.97/0.98$) and amount up to 8.3%/10.5% (from March to September). The bottom panel of Fig. 5 indicates that the CSC is sensitive to changes in LAI ($R = -0.88$), even though this sensitiv-
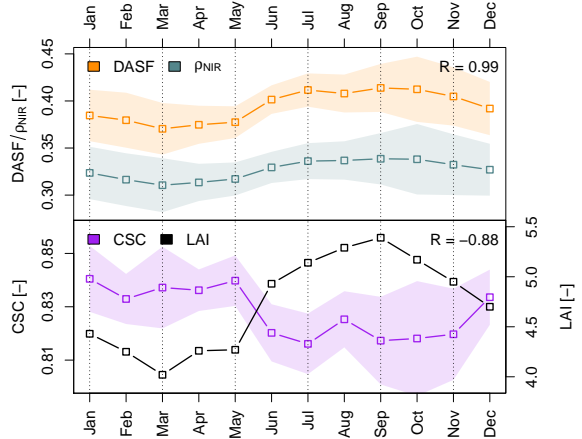

Figure 5: ρ_{NIR} (upper panel, blue), DASF (upper panel, orange), and CSC (bottom panel, purple) computed from simulated data for a realistic tropical forest observed under a simplified GOME-2 sun-sensor geometry. The standard deviations (shaded areas) result from two relative azimuth angles and 14 viewing zenith angles (value depends on month, see Fig. 3). The LAI input value (bottom panel, black) corresponds to the monthly average of the study domain for 2014.

ity is rather low. There is a 25% increase in LAI from March to September, which translates into a 2.9% decrease in CSC. The low sensitivity can be explained by the asymptotic behavior of the recollision probability, which reflects the saturation effect in dense vegetation canopies. A significant impact of viewing zenith angle variations on absolute CSC values has not been found, but the standard deviation increases with viewing zenith angles.

4 Results & Discussion

4.1 Spatiotemporal Composites

We performed global DASF retrievals from GOME-2 soundings with relative cloud fractions (from FRESCO, Wang et al., 2008) below 0.5 for the 08/2013-08/2016 time period. The processed data can be retrieved from `http://is.gd/GOME_2_DASF`. As described in Sect. 2.5.1, the R^2 value of the underlying linear fit Eq. (8) is a measure of retrieval quality and applicability of assumptions. We have therefore tested different R^2 value thresholds to examine the impact on resulting composites. In general, it appeared that non-vegetated areas and regions with sparse vegetation (e.g.,
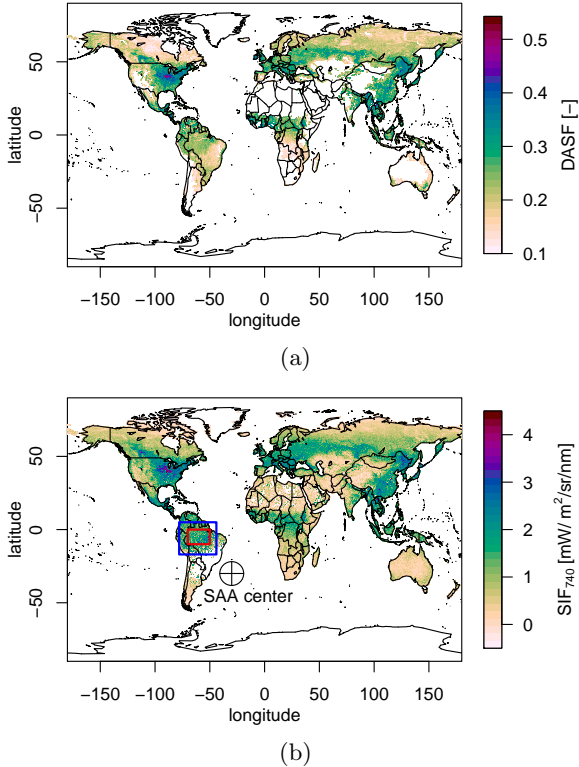
(a)

(b)

Figure 6: Monthly (a) DASF($R^2 >= 0.9$) and (b) SIF composites for July 2014 on a 0.2° x 0.2° grid derived from GOME-2 soundings with relative cloud fractions (from FRESCO, Wang et al., 2008) below 0.5. The center of the SAA at 40°W and 30°S, the extent of the region shown in Fig. 1, 7 (blue) and our study domain (red) are in addition depicted in map (b).

deserts and ice sheets) are masked by a R^2 value above 0.7. It has emerged that a more stringent R^2 filter criterion also results in reduced relative cloud fraction averages:

1. $R^2 > 0.7$: 7.4% of remaining soundings own a cloud fraction larger than 0.3

2. $R^2 > 0.9$: 3.5% of remaining soundings own a cloud fraction larger than 0.3

Global monthly composites of DASF($R^2 >= 0.9$) and GOME-2 SIF for July 2014 on a 0.2° x 0.2° grid are shown in Fig. 6. It is interesting to note the high DASF and SIF average in northern mid-latitudes with peak values in the US Corn Belt region. This peak in SIF and DASF in large cropland and grassland areas might be explained by the rather less complex vegetation structure associated with an enhanced escape probability for scattered/emitted photons. Equally remarkable is that spatial DASF patterns apparently reproduce spatial SIF averages. This characteristic can be attributed

to a similar sensitivity to canopy structure and illumination conditions. For example, a complex canopy structure leads to enhanced multiple scattering by which less photons escape regardless whether photons originate from the sun or from SIF.

Even though the ratio ρ_{NIR}/DASF (CSC) appears to be robust against cloud contamination (see Sect. 3.1), we performed the further analysis on DASF retrievals with a R^2 value above 0.9 in combination with a strict cloud filter (cloud fraction equal zero) to ensure that the impact of clouds is as low as possible. Fig. 7 depicts composites of CSC, SIF, and NDVI derived from GOME-2 data in the Amazon region for the July–September 2014 period. The MODIS NDVI (MYD13C1, 2016) composite for the same time period illustrates the largely consistent spatial patterns as well as consistent absolute values with respect to the GOME-2 NDVI composite. Both composites clearly demonstrate the saturation effect of the NDVI in dense vegetation canopies. The consistency is particularly remarkable against the background of a considerable difference in the spectral and spatial sampling of the satellite instruments. While spectral broadband measurements in channel 1 (red band: 620–670 nm) and channel 2 (NIR band: 841–876 nm) with a fine spatial sampling of 250 m form the basis to compute the NDVI in case of MODIS, we used 2 subsets of the fourth channel from the GOME-2 instrument (660–665 nm, 780–785 nm) with a large ground pixel size of 40 km x 40 km for the same purpose.

In view of the sensitivity of CSC to the canopy p value (Eq. 10) and subsequently to the LAI (Sect. 3.2), it seems reasonable that grasslands and savannas (see Fig. 1 for the regional land cover distribution) reach high, partly saturated CSC levels, while evergreen broadleaf forest regions are clearly separated through lower CSC values. In contrast to the NDVI, the saturation effect appears to be reversed - the CSC saturates in regions covered by less dense vegetation. This supports the CSC as a valuable vegetation parameter particularly for dense vegetation canopies such as the Amazon forests. The GOME-2 SIF composite in Fig. 7b also reveals a few interesting aspects. First, a spatially highly variable structure can
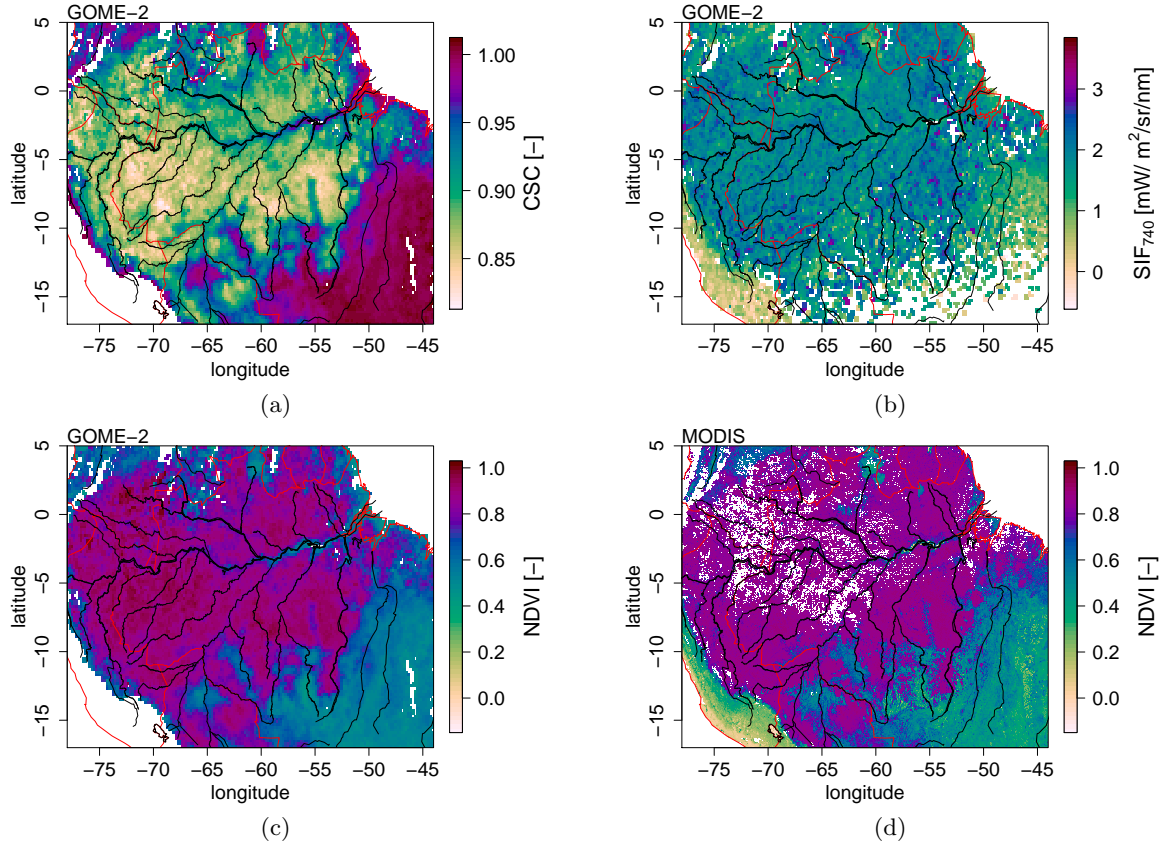
13

Figure 7: Composites of (a) CSC, (b) SIF, and (c) NDVI derived from GOME-2 data with relative cloud fractions equal zero for the July–September 2014 period on a 0.2° x 0.2° grid in the Amazon region. Figure (d) shows a MODIS NDVI composite (MYD13C1, 2016, see Sect. 2.8) on a 0.05° x 0.05° grid for the same time period. White areas indicate missing values. The spatial sampling of CSC is consistent with that of GOME-2 NDVI, missing values are primarily due to underlying DASF retrievals with $R^2 < 0.9$ (see Sect. 2.5.1). Missing values in the GOME-2 SIF composite are mostly due to our restrictive RSS filter criterion in order to reduce the impact of the SAA (see Sect. 2.3.1).

be observed, which might indicate an elevated noise level or may point to a high degree of spatial heterogeneity in the SIF emission. As mentioned in Sect. 2.3.1, we reduced the impact of the SAA on GOME-2 SIF by a restrictive filtering of potentially corrupted retrievals. This lead to a concentrated appearance of missing values in south-eastern regions of the shown region. The large extent of the affected region on the South American continent can be seen from the global composite in Fig. 6b. Although the SAA represents a limiting factor, remaining grid cells in Fig. 7b reveal reasonable SIF averages with respect to the land cover distribution. For example, sparsely vegetated areas at Peru's largely arid Pacific coast and the Andes mountains (south-western sector of the map) show SIF values consistently close to zero.

4.2 Comparison between SIF from OCO-2 & GOME-2

This section addresses the question of whether SIF from GOME-2 data is consistent with SIF from OCO-2 data. Fig. 8 depicts monthly SIF averages from both instruments for our study domain. We will discuss a few properties and assumptions, which complicate comparisons in the following paragraph.

First, it should be noted that the spatial coverage is substantially limited since only grid cells, which contain SIF retrievals from both OCO-2 and GOME-2 measurements are compared. Additionally, GOME-2 measurements have been filtered for soundings with viewing zenith angles lower than 10° to match OCO-2 nadir observations. The cloud filter threshold of GOME-2 SIF retrievals had to be relaxed (maximum cloud fraction is 0.5, mean cloud fraction is 0.11) to ensure that there are over-
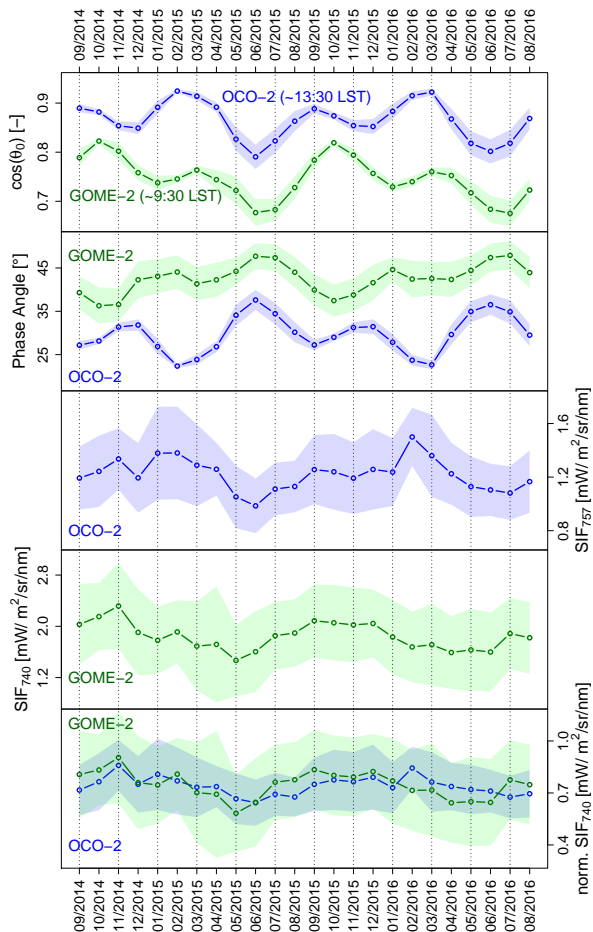
Figure 8: Comparison of the cosine of the solar zenith angle (θ_0), phase angle, SIF and normalized (daily illumination cycle and wavelength corrected) SIF_{740} from OCO-2 (blue) and GOME-2 (green). Only study domain grid cells which contain SIF retrievals from both instruments form the basis of the shown monthly averages. Additionally, GOME-2 time series have been filtered for soundings with viewing zenith angles lower than $10°$ to match OCO-2 nadir observations. Shaded areas indicate the spatial standard deviation.

lapping regions in all evaluated months. Köhler et al. (2015b) have shown (for a similar area) that absolute SIF values decrease by relaxing the cloud filter threshold, while the temporal pattern remains almost unaffected. This can also be concluded from Fig. 10 in Sect. 4.4. However, the number of overlapping grid cells per month is rather low and ranges from 16-368, which corresponds to 0.4%-10% of total grid cells. It might also be considered that absolute SIF values are expected to be different, which is primarily due to different overpass times (GOME-2: ~9:30 LST, OCO-2: ~13:30 LST) and evaluated wavelengths (GOME-2: 740 nm, OCO-2: 757 nm).

The most obvious difference in the time se-

ries lies in the seasonal cycle, which highlights the instantaneous nature of the SIF signal, i.e. the annual maximum of SIF retrieved from OCO-2 occurs in February, while the maximum SIF obtained from GOME-2 data is observed around October. Both SIF time series roughly follow the course of illumination, while annual peak values coincide with the associated maximum of the cosine of the solar zenith angle, which can be regarded as a proxy for instantaneous PAR (under cloud free conditions), and the minimum of the average phase angle. Considering the relaxed cloud filter in case of SIF from GOME-2 and the maximum of OCO-2 SIF during the wet season, it is remarkable that the large agreement of SIF with instantaneous PAR seem to discard a seasonality being driven by clouds. The OCO-2 SIF time series seems to be out of the illumination phase only in October and November 2014 where SIF values slightly increase, while instantaneous PAR declines (proxied by the cosine of the solar zenith angle). A similar feature is present in the GOME-2 SIF time series, where the high November 2014 SIF average is not explained by illumination.

The bottom panel of Fig. 8 shows the normalized SIF time series, corrected for the different evaluated wavelengths and overpass times (see Sect. 2.3.3). Both time series agree very well in terms of absolute values and covering seasonal swings, while a high level of normalized SIF is maintained throughout the covered time period.

In summary, OCO-2 and GOME-2 SIF show consistent seasonal cycles driven by instantaneous PAR, clearly demonstrating the need to consider the time of measurement in addition to the observation geometry.

4.3 Directional Effects

The necessity to address the sun-surface-sensor geometry arises from anisotropic reflectance characteristics of natural surfaces, also known as directional effects. It has already been proven that a significant impact on reflectance data (which consequently translates into VIs) complicates the interpretation of satellite remote sensing products, particularly in the Amazon rainforest (Maeda and Galvão, 2015; Hilker et al., 2015). Simulations (van der Tol
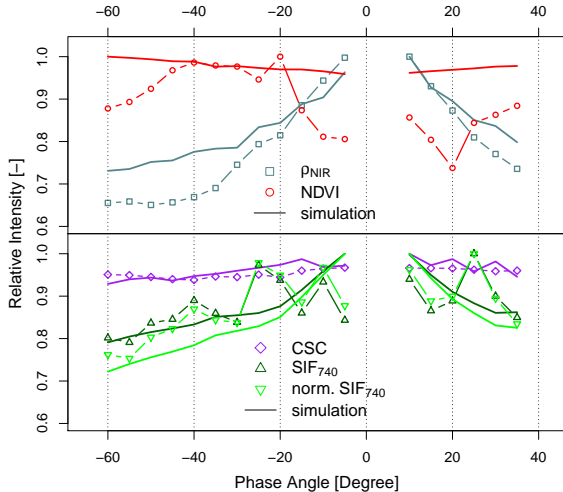
Figure 9: Relative intensity of NIR, NDVI, CSC, SIF and normalized SIF as a function of phase angle. Underlying absolute values of broken lines are averages derived from GOME-2 data in the study domain for October 2014, sampled in 5° phase angle steps. The solid lines depict relative intensities computed from FLiES simulations based on the average SZA, VZA, LAI and RAA per phase angle step.

et al., 2009) and measurements (Liu et al., 2016) at the TOC level reveal that SIF is also subject to the hot spot effect. Guanter et al. (2012) have shown that even satellite-based SIF measurements from GOSAT data are strongly affected by directional effects. Therefore, it is reasonable to examine the sensitivity of GOME-2 SIF to view-illumination effects, which previously has not been considered.

A wide range of phase angles from GOME-2 observations within the study domain occurs in October (see Fig. 9) and provides the opportunity to estimate and compare intensities and characteristics of directional effects on all retrieved vegetation parameters. Although there is a lack of a controlled environment and a certain level of change may be anticipated, we assume that the canopy remains sufficiently invariant during one month and that the study domain is fairly homogeneous to tentatively estimate the directional effects. Fig. 9 depicts relative intensities of ρ_{NIR}, NDVI, CSC, SIF and normalized SIF for simulated and real GOME-2 data as a function of phase angle in October 2014. It has emerged that the FRESCO algorithm preferentially detects higher effective cloud fractions when the phase angle approaches 0°. We therefore relaxed the cloud filter threshold in a similar way to Sect. 4.2 (av-

erage cloud fraction is 0.11) in order to cover the largest possible phase angle range.

Overall, our results confirm that NIR reflectance is significantly affected by phase angle variations (e.g., Maeda and Galvão, 2015). In particular, the NIR reflectance shape illustrates the hot spot effect, which exhibits the most pronounced directional effect among the tested parameters (intensity varies within 35%). The FLiES simulations show a slightly less pronounced effect on NIR reflectance, which might be due to the challenge of modeling the reflectance around the hot spot region. More specifically, the modeled reflectance may have limitations because of a lack of detailed forest structure information with respect to the Amazon forest. A less clear directionality is visible in the NDVI-phase angle dependency. Values tend to decrease with lower absolute phase angles, while the substantial variation amounts up to 30%. With the simulated NDVI and its sensitivity to cloud effects (Sect. 3.1), it can be anticipated that this behavior results from cloud contaminated GOME-2 footprints. Compared to NIR reflectance and NDVI, SIF seems to be significantly less affected by changing phase angles (intensity changes are in the order of 20%, change in terms of absolute values amounts up to 0.5 mW m^{-2} sr^{-1} nm^{-1}). Nevertheless, there appears to be a tendency for higher SIF values towards 0° phase angle, which is in agreement with our FLiES simulations. The fluctuations in our SIF observations might be caused by noise and/or a high variability in fluorescence yields across the forest canopy. This similar directionality as observed in simulations (van der Tol et al., 2009) and GOSAT SIF data (Guanter et al., 2012) confirms that there is a similar hot spot effect compared to NIR reflectance. The actual magnitude of this effect might even be larger because the solar zenith angle increases (from $\sim 31°$ to $\sim 39°$) with decreasing absolute phase angle values (not shown). Accordingly, a decline of SIF values could be expected because of the decrease in instantaneous PAR with inclined illumination angles. However, the opposite behavior is observed, which suggests that the hot spot effect overcompensates the slight decrease in illumination. It should be noted that this effect is even amplified by normaliz-

16

ing SIF, resulting in intensity changes slightly above 20%. Seasonal changes in average phase angles will therefore likely affect the SIF time series in our study domain if they are not accounted for. In contrast to the previously evaluated parameters, it is remarkable that CSC is almost unaffected by phase angle variations as predicted by theory (Sect. 2.5). This characteristic combined with the benefit of being highly independent of atmospheric effects (Sect. 3.1) makes CSC a promising tool for the monitoring of leaf properties in dense canopies. However, the remaining sensitivity to canopy structure as suggested by our sensitivity analysis is a limiting factor regarding the assessment of actual leaf properties.

4.4 Large-Scale Vegetation Dynamics

The persistence of recurring phase angles in GOME-2 observations (see Fig. 3) allows us to suppress seasonal changes in sun-sensor geometry by limiting the phase angle range. By contrast, OCO-2 observations are subject to an inseparable seasonality in average phase angle values (not explicitly shown, but essentially consistent with the course shown in the second panel of Fig. 8). For this reason, we focus on retrieved vegetation parameters from phase angle limited (between $-65°$ and $-40°$) GOME-2 measurements in this section.

Fig. 10 depicts long-term monthly averages from August 2013 to August 2016 of computed vegetation parameters (SIF, normalized SIF, CSC and NDVI) and of environmental conditions (PAR, precipitation, LAI) within our study domain (Sect. 2.2). The spatial coverage of each month is also depicted in Fig. 10 where differences for the retrieved vegetation parameters arise from individual filter criteria.

The strict/relaxed filter (denoted by circles/crosses) constrains all underlying measurements to own a relative cloud fraction equal 0/below 0.5. In addition, SIF (strict filter) and NDVI retrievals are only included if the phase angle ranges between $-65°$ and $-40°$. The phase angle restriction is not necessary for CSC as it can be concluded from Fig. 9. However, the number of selected CSC retrievals might be reduced through the quality filter of the underlying DASF computation ($R^2 > 0.9$, see

2.5.1). The remaining SIF retrievals (strict filter) result in the lowest spatial coverage, which is mainly due to the restrictive RSS threshold (see Sect. 2.3.1).

Fig. 10 reveals that the spatial coverage is reduced during months with intense precipitation. The supplementary data sets have therefore been collocated with valid SIF grid cells (strict filter) to avoid a spatial mismatch, while monthly averages for the entire study domain are denoted by triangles. The minor differences between the sparsest (SIF) and the full spatial coverage for the supplementary data sets suggest that the spatial sampling is sufficiently representative for the entire study domain. Nevertheless, it should be noted that the coverage of SIF observations (strict filter) is reduced to about 50% for the average in March.

In contrast to Fig. 8 (evaluating only grid cells which contain retrievals from both OCO-2 and GOME-2), two annual peaks can be observed in the SIF time series. The maximum in October can be linked to the maximum in PAR, while the lower peak around January/February is not explained by the shown environmental variables. It seems that the SIF time series is a superposition of monthly averaged PAR (based on 3-hourly data, R=0.84) and an additional seasonality. In view of the comparison between OCO-2 and GOME-2 SIF (Sect. 4.2), it is remarkable that the illumination conditions at the overpass time of GOME-2 (9:30 LST) track seasonal variations of instantaneous as well as monthly PAR. As expected, the time series is consistently higher than the one using a relaxed cloud filter. Slightly larger deviations arise during the wet season, which might be explained by the abundance of clouds. The magnitude of seasonal swings in SIF amounts up to 21% (27% for the relaxed filtering) with regard to the annual maximum.

The normalization of SIF emphasizes the peak around January/February (wet season), which now represents the annual maximum. Interestingly, the peak of the simulated, normalized SIF time series can still be observed at the end of the dry season (September), reflecting the response to variations in LAI and observation geometry only. We hypothesize that the observed seasonality might be explained by a combination of effects, some of which have
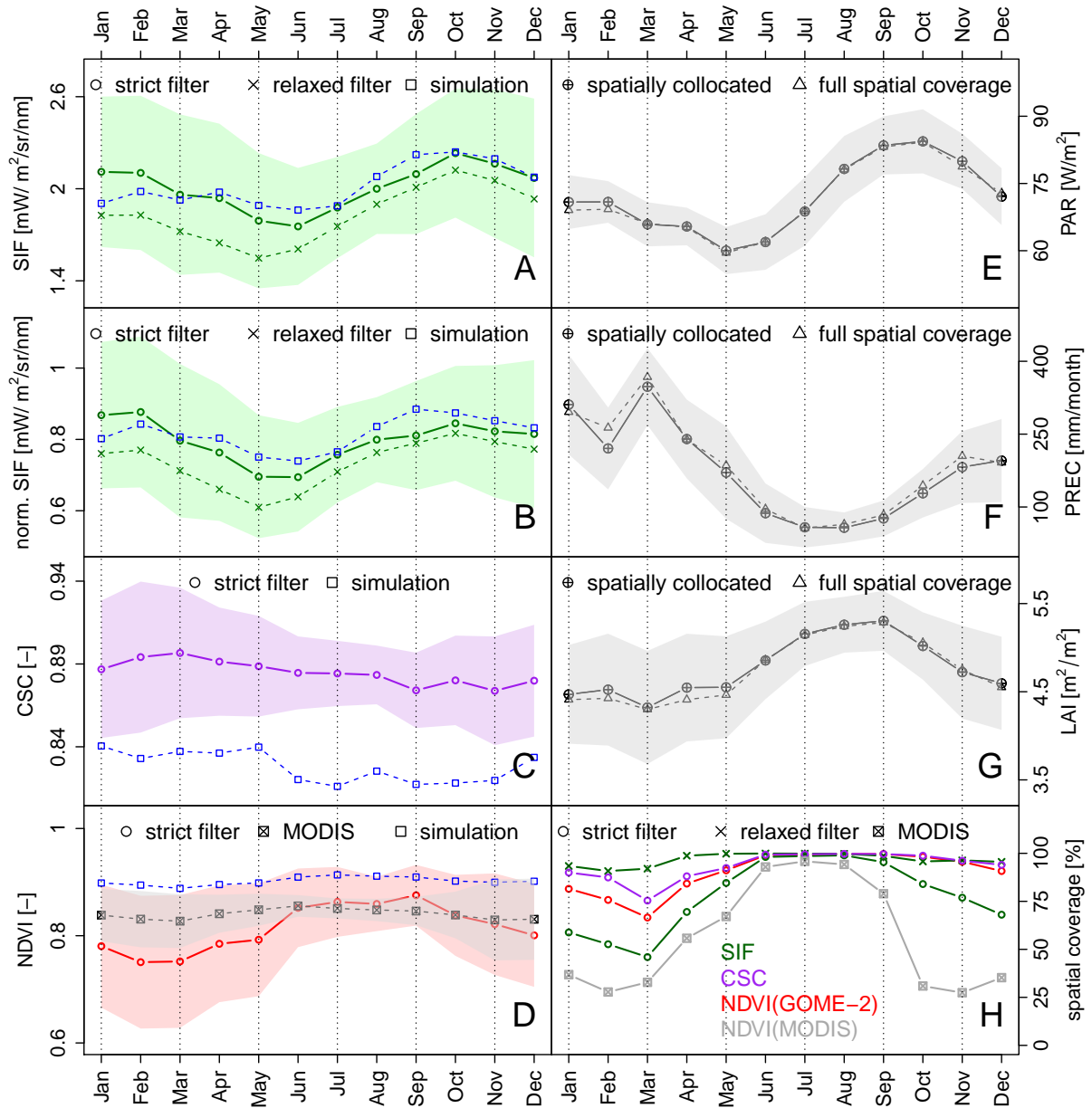
Figure 10: Long-term monthly averages (August 2013 – August 2016) of A) SIF (green), B) normalized SIF (green), C) CSC (purple), and D) NDVI (red) retrieved from GOME-2 data together with simulation results (blue) and MODIS NDVI (MYD13C1, 2016, black). The strict (relaxed) filter indicates that underlying measurements own a cloud fraction equal to 0 (below 0.5) and phase angles between $-65°$ and $-40°$ (except for CSC). The simulations of a realistic tropical forest landscape are subject to following boundary conditions: simplified GOME-2 like sun-sensor geometry, cloud free sky, monthly LAI averages for 2014. In addition, averages of E) PAR (based on 3-hourly data), F) precipitation, and G) LAI from supplementary data sets are depicted in black, where circles (triangles) indicate a spatial collocation (full spatial coverage) with respect to the spatial coverage of SIF. Spatial standard deviations are depicted by shaded areas.

recently attracted attention: i) variations in vertical canopy structure (Tang and Dubayah, 2017), and ii) leaf age effects (Wu et al., 2016). First, the wet season peak could result from fewer gaps in the canopy during this time of year (Tang and Dubayah, 2017), meaning that most of the detected SIF signal emanates from sunlit leaves in the uppermost vegetation layer. This might go along with a leaf-age distribution shifted toward mature leaves, which appear to have a higher photosynthetic capacity than flushing and old leaves (Wu et al., 2016). Second, the annual dip during the early dry season (May and June) might be driven by flushing leaves in combination with an increased gap density in the canopy, whereby more shaded leaves (emitting less SIF) are observed. Finally, the adjacent increase in normalized SIF could be explained by increasing understory LAI (Tang and Dubayah, 2017), decreasing gap density (Tang and Dubayah, 2017), and increasing the number of mature leaves (Wu et al., 2016), water availability, and PAR coincidentally.

The seasonality of CSC is less variable (intensity change amounts up to 3%), and reveals a peak in March and minimum in September. The CSC time series is weakly anti-correlated with LAI (R=-0.64) and equally weak positively correlated with the amount of precipitation (R=0.58). Although the sensitivity to LAI and cloud contamination appeared to be small, the low variability of CSC could entirely be controlled by these effects (LAI: 3%, cloud contamination:0-3%).

The NDVI simulation results (with constant leaf, wood and soil properties; LAI > 4) and the MODIS NDVI indicate that the sensitivity of NDVI to LAI is almost saturated. At the same time, results from our sensitivity analysis (Sect. 3.1) and previous investigations (e.g., Kobayashi and Dye, 2005; Hilker et al., 2015) demonstrate the strong sensitivity to atmospheric conditions. Hence, it seems likely that the GOME-2 NDVI time series is dominated by undetected sub-pixel clouds, which in turn may point to an insufficient cloud filtering.

5 Summary

We have evaluated two new vegetation parameters, SIF and CSC, with respect to their prospects and drawbacks for the monitoring of vegetation dynamics and productivity in the central Amazon Basin. For this purpose, we have used data derived from currently operating satellite sensors as well as simulated data from the MOMO and the FLiES radiative transfer models.

The comparison between OCO-2 and GOME-2 SIF emphasizes the instantaneous nature of SIF measurements. The annual cycle is closely related to illumination conditions at the overpass time (instantaneous PAR). To this end, OCO-2 and GOME-2 SIF show consistent seasonal cycles, and a strong agreement in terms of absolute values when correcting SIF for differences in illumination angle and wavelength. We have illustrated that the seasonality of daily averaged illumination is in general not represented by the seasonality of instantaneous illumination. The GOME-2 overpass time around 9:30 LST appears to be an exception, its seasonality is indeed representative for variations in PAR (based on 3-hourly data) on the monthly time scale. A drawback of using SIF in the Amazon region arises from the South Atlantic Anomaly, as increased noise requires a strict filtering and leads to a considerably reduced number of reliable SIF retrievals. Nevertheless, large-scale averages of GOME-2 SIF reveal two distinct contributions to the seasonality of photosynthetic activity. First, the dominant seasonality is associated with variations in PAR with a peak in October. Second, a peak around January/February indicates an increase in photosynthetic activity, which is not directly linked to seasonal variations in PAR or precipitation and may be associated with leaf age effects and variations in the vertical canopy structure. The wet season peak becomes even more pronounced (forming the annual maximum) as SIF is normalized. Our analysis of phase angle effects provides evidence for a significant impact of the hot spot effect on GOME-2 SIF data.

Contrastingly, CSC appears to be highly independent of sun-sensor geometry or atmospheric effects. Compared to NDVI, a major

benefit of CSC for the monitoring of dense vegetation lies in the reversed saturation. However, the slight response to LAI variations limits the informative value regarding the assessment of actual leaf properties. We have found an overall low variability of CSC from GOME-2 data within the central Amazon Basin, while a relatively high spatial standard deviation points to a high degree of spatial heterogeneity. Nevertheless, it should be noted that the seasonality of CSC could also be explained by cloud contamination in combination with variations in LAI.

The frequent cloud cover in tropical rainforests in combination with the relatively large pixel size of GOME-2 complicates the analysis, because undetected sub-pixel clouds and areas of less dense vegetation are likely to occur. The comparison between GOME-2 NDVI and simulated/MODIS NDVI suggests that cloud contamination represents the most limiting factor of our study, although both SIF and CSC are significantly less affected by fractional cloud-cover than traditional VIs. However, further studies are needed to fully exploit the potential of space-based SIF and CSC observations in the Amazon region. Even though OCO-2 already provides a fine spatial sampling in case of SIF, it is nevertheless crucial that simultaneous and spatially continuous retrievals of both SIF and CSC will also be possible for the next generation of satellite instruments with a similar spectral resolution/coverage as GOME-2. These instruments/satellites include the TROPOspheric Monitoring Instrument (TROPOMI; 7 km x 7 km, Veefkind et al., 2012) and the FLuorescence EXplorer (FLEX, 0.3 km x 0.3 km; Rascher et al., 2008).

Acknowledgement

References

Baret, F., Weiss, M., Lacaze, R., Camacho, F., Makhmara, H., Pacholcyzk, P., Smets, B., 2013. GEOV1: LAI and FAPAR essential climate variables and FCOVER global time series capitalizing over existing products. Part1: Principles of development and production. Remote Sensing of Environment 137, 299–309.

Bi, J., Knyazikhin, Y., Choi, S., Park, T., Barichivich, J., Ciais, P., Fu, R., Ganguly, S., Hall, F., Hilker, T., et al., 2015. Sunlight mediated seasonality in canopy structure and photosynthetic activity of Amazonian rainforests. Environmental Research Letters 10 (6), 064014.

Carswell, F., Meir, P., Wandelli, E., Bonates, L., Kruijt, B., Barbosa, E., Nobre, A., Grace, J., Jarvis, P., et al., 2000. Photosynthetic capacity in a central amazonian rain forest. Tree Physiology 20 (3), 179–186.

Damm, A., Guanter, L., Verhoef, W., Schläpfer, D., Garbari, S., Schaepman, M., 2015. Impact of varying irradiance on vegetation indices and chlorophyll fluorescence derived from spectroscopy data. Remote Sensing of Environment 156, 202–215.

Dee, D., Uppala, S., Simmons, A., Berrisford, P., Poli, P., Kobayashi, S., Andrae, U., Balmaseda, M., Balsamo, G., Bauer, P., et al., 2011. The ERA-Interim reanalysis: Configuration and performance of the data assimilation system. Quarterly Journal of the Royal Meteorological Society 137 (656), 553–597.

Farquhar, G. v., von Caemmerer, S. v., Berry, J., 1980. A biochemical model of photosynthetic co2 assimilation in leaves of c3 species. Planta 149 (1), 78–90.

Fell, F., Fischer, J., 2001. Numerical simulation of the light field in the atmosphere–ocean system using the matrix-operator method. Journal of Quantitative Spectroscopy and Radiative Transfer 69 (3), 351–388.

Frankenberg, C., Butz, A., Toon, G., 2011a. Disentangling chlorophyll fluorescence from atmospheric scattering effects in O2 A-band spectra of reflected sun-light. Geophysical Research Letters 38 (3).

Frankenberg, C., Fisher, J. B., Worden, J., Badgley, G., Saatchi, S. S., Lee, J.-E., Toon, G. C., Butz, A., Jung, M., Kuze, A., et al., 2011b. New global observations of the terrestrial carbon cycle from GOSAT: Patterns of plant fluorescence with gross primary productivity. Geophysical Research Letters 38 (17).

Frankenberg, C., O'Dell, C., Berry, J., Guanter, L., Joiner, J., Köhler, P., Pollock, R., Taylor, T. E., 2014. Prospects for chlorophyll fluorescence remote sensing from the Orbiting Carbon Observatory-2. Remote Sensing of Environment 147, 1–12.

Frankenberg, C., O'Dell, C., Guanter, L., McDuffie, J., 2012. Remote sensing of near-infrared chlorophyll fluorescence from space in scattering atmospheres: implications for its retrieval and interferences with atmospheric CO2 retrievals. Atmospheric Measurement Techniques 5 (8), 2081–2094.

Friedl, M. A., McIver, D. K., Hodges, J. C., Zhang, X., Muchoney, D., Strahler, A. H., Woodcock, C. E., Gopal, S., Schneider, A., Cooper, A., et al., 2002. Global land cover mapping from MODIS: algorithms and early results. Remote Sensing of Environment 83 (1), 287–302.

Guan, K., Pan, M., Li, H., Wolf, A., Wu, J., Medvigy, D., Caylor, K. K., Sheffield, J., Wood, E. F., Malhi, Y., et al., 2015. Photosynthetic seasonality of global tropical forests constrained by hydroclimate. Nature Geoscience 8 (4), 284–289.

Guanter, L., Aben, I., Tol, P., Krijger, J., Hollstein, A., Köhler, P., Damm, A., Joiner, J., Frankenberg, C., Landgraf, J., 2015. Potential of the TROPOspheric Monitoring Instrument (TROPOMI) onboard the Sentinel-5 Precursor for the monitoring of terrestrial chlorophyll fluorescence. Atmospheric Measurement Techniques 8 (3), 1337–1352.

Guanter, L., Frankenberg, C., Dudhia, A., Lewis, P. E., Gómez-Dans, J., Kuze, A., Suto, H., Grainger, R. G., 2012. Retrieval and global assessment of terrestrial chlorophyll fluorescence from GOSAT space measurements. Remote Sensing of Environment 121, 236–251.

Hapke, B., 2012. Theory of reflectance and emittance spectroscopy. Cambridge University Press.

Hikosaka, K., Niinemets, Ü., Anten, N. P., 2015. Canopy Photosynthesis: From Basics to Applications.

Hilker, T., Lyapustin, A. I., Hall, F. G., Myneni, R., Knyazikhin, Y., Wang, Y., Tucker, C. J., Sellers, P. J., 2015. On the measurability of change in Amazon vegetation from MODIS. Remote Sensing of Environment 166, 233–242.

Hu, B., Lucht, W., Strahler, A. H., 1999. The interrelationship of atmospheric correction of reflectances and surface BRDF retrieval: A sensitivity study. Geoscience and Remote Sensing, IEEE Transactions on 37 (2), 724–738.

Huang, D., Knyazikhin, Y., Dickinson, R. E., Rautiainen, M., Stenberg, P., Disney, M., Lewis, P., Cescatti, A., Tian, Y., Verhoef, W., et al., 2007. Canopy spectral invariants for remote sensing and model applications. Remote Sensing of Environment 106 (1), 106–122.

Huete, A. R., Didan, K., Shimabukuro, Y. E., Ratana, P., Saleska, S. R., Hutyra, L. R., Yang, W., Nemani, R. R., Myneni, R., 2006. Amazon rainforests green-up with sunlight in dry season. Geophysical Research Letters 33 (6).

Joiner, J., Guanter, L., Lindstrot, R., Voigt, M., Vasilkov, A., Middleton, E., Huemmrich, K., Yoshida, Y., Frankenberg, C., 2013. Global monitoring of terrestrial chlorophyll fluorescence from moderate-spectral-resolution near-infrared satellite measurements: methodology, simulations, and application to GOME-2. Atmospheric Measurement Techniques 6 (10), 2803–2823.

Joiner, J., Yoshida, Y., Vasilkov, A., Middleton, E., Campbell, P., Kuze, A., et al., 2012. Filling-in of near-infrared solar lines by terrestrial fluorescence and other geophysical effects: Simulations and space-based observations from SCIAMACHY and GOSAT. Atmospheric Measurement Techniques 5 (4), 809–829.

Joiner, J., Yoshida, Y., Vasilkov, A., Middleton, E., et al., 2011. First observations of global and seasonal terrestrial chlorophyll fluorescence from space. Biogeosciences 8 (3), 637–651.

Knyazikhin, Y., Kranigk, J., Myneni, R. B., Panfyorov, O., Gravenhorst, G., 1998. Influence of small-scale structure on radiative transfer and photosynthesis in vegetation canopies. Journal of Geophysical Research: Atmospheres (1984–2012) 103 (D6), 6133–6144.

Knyazikhin, Y., Schull, M. A., Stenberg, P., Mttus, M., Rautiainen, M., Yang, Y., Marshak, A., Latorre Carmona, P., Kaufmann, R. K., Lewis, P., Disney, M. I., Vanderbilt, V., Davis, A. B., Baret, F., Jacquemoud, S., Lyapustin, A., Myneni, R. B., 2013. Hyperspectral remote sensing of foliar nitrogen content. Proceedings of the National Academy of Sciences 110 (3), E185E192.

Knyazikhin, Y., Schull, M. A., Xu, L., Myneni, R. B., Samanta, A., 2011. Canopy spectral invariants. Part 1: A new concept in remote sensing of vegetation. Journal of Quantitative Spectroscopy and Radiative Transfer 112 (4), 727–735.

Kobayashi, H., 2015a. Directional effect of canopy scale sun-induced chlorophyll fluorescence: Theoretical Consideration in A3-D radiative transfer model. In: Geoscience and Remote Sensing Symposium (IGARSS), 2015 IEEE International. IEEE, pp. 3413–3415.

Kobayashi, H., 2015b. Leaf, woody and background optical data for GCOM-C LAI/FAPAR retrieval. JAXA GCOM-C RA4 #102 project documents, available from the author upon the request.

Kobayashi, H., Dye, D. G., 2005. Atmospheric conditions for monitoring the long-term vegetation dynamics in the Amazon using normalized difference vegetation index. Remote Sensing of Environment 97 (4), 519–525.

Kobayashi, H., Iwabuchi, H., 2008. A coupled 1-D atmosphere and 3-D canopy radiative transfer model for canopy reflectance, light environment, and photosynthesis simulation in a heterogeneous landscape. Remote Sensing of Environment 112 (1), 173–185.

Köhler, P., Guanter, L., Frankenberg, C., July 2015a. Simplified Physically Based Retrieval of Sun-Induced Chlorophyll Fluorescence From GOSAT Data. Geoscience and Remote Sensing Letters, IEEE 12 (7), 1446–1450.

Köhler, P., Guanter, L., Joiner, J., 2015b. A linear method for the retrieval of sun-induced chlorophyll fluorescence from GOME-2 and SCIAMACHY data. Atmospheric Measurement Techniques 8 (6), 2589–2608.

Lee, J.-E., Frankenberg, C., van der Tol, C., Berry, J. A., Guanter, L., Boyce, C. K., Fisher, J. B., Morrow, E., Worden, J. R., Asefi, S., Badgley, G., Saatchi, S., 2013. Forest productivity and water stress in Amazonia: observations from GOSAT chlorophyll fluorescence. Proceedings of the Royal Society of London B: Biological Sciences 280 (1761).

Lewis, P., Disney, M., 2007. Spectral invariants and scattering across multiple scales from within-leaf to canopy. Remote Sensing of Environment 109 (2), 196–206.

Liu, L., Liu, X., Wang, Z., Zhang, B., 2016. Measurement and Analysis of Bidirectional SIF Emissions in Wheat Canopies. IEEE Transactions on Geoscience and Remote Sensing 54 (5), 2640–2651.

MACC, 2016. Monitoring Atmospheric Composition and Climate. Available online: `http://www.gmes-atmosphere.eu`.

Maeda, E. E., Galvão, L. S., 2015. Sun-sensor geometry effects on vegetation index anomalies in the Amazon rainforest. GIScience & Remote Sensing 52 (3), 332–343.

Magney, T. S., Frankenberg, C., Fisher, J. B., Sun, Y., North, G. B., Davis, T. S., Kornfeld, A., Siebke, K., 2017. Connecting active to passive fluorescence with photosynthesis: a method for evaluating remote sensing measurements of Chl fluorescence. New Phytologist 215 (4), 1594–1608.

Morton, D. C., Nagol, J., Carabajal, C. C., Rosette, J., Palace, M., Cook, B. D., Vermote, E. F., Harding, D. J., North, P. R., 2014. Amazon forests maintain consistent canopy structure and greenness during the dry season. Nature 506 (7487), 221–224.

Munro, R., Eisinger, M., Anderson, C., Callies, J., Corpaccioli, E., Lang, R., Lefebvre, A., Livschitz, Y., Albiñana, A. P., 2006. GOME-2 on MetOp. In: Proc. of The 2006 EUMETSAT Meteorological Satellite Conference, Helsinki, Finland. pp. 12–16.

MYD13C1, 2016. Vegetation Indices 16-Day L3 Global 0.05Deg CMG. Available online: `https://lpdaac.usgs.gov/dataset_discovery/modis/modis_products_table/mod13c1`.

Parazoo, N. C., Bowman, K., Frankenberg, C., Lee, J.-E., Fisher, J. B., Worden, J., Jones, D., Berry, J., Collatz, G. J., Baker, I. T., et al., 2013. Interpreting seasonal changes in the carbon balance of southern Amazonia using measurements of XCO2 and chlorophyll fluorescence from GOSAT. Geophysical Research Letters 40 (11), 2829–2833.

Pedrós, R., Goulas, Y., Jacquemoud, S., Louis, J., Moya, I., 2010. Fluormodleaf: A new leaf fluorescence emission model based on the prospect model. Remote Sensing of Environment 114 (1), 155–167.

Rascher, U., Gioli, B., Miglietta, F., 2008. Flexfluorescence explorer: a remote sensing approach to quantify spatio-temporal variations of photosynthetic efficiency from space. In: Photosynthesis. Energy from the Sun. Springer, pp. 1387–1390.

Roberts, D., Nelson, B., Adams, J., Palmer, F., 1998. Spectral changes with leaf aging in Amazon caatinga. Trees 12 (6), 315–325.

Samanta, A., Knyazikhin, Y., Xu, L., Dickinson, R. E., Fu, R., Costa, M. H., Saatchi, S. S., Nemani, R. R., Myneni, R. B., 2012. Seasonal changes in leaf area of Amazon forests from leaf flushing and abscission. Journal of Geophysical Research: Biogeosciences 117 (G1), g01015.

Schull, M. A., Knyazikhin, Y., Xu, L., Samanta, A., Carmona, P. L., Lepine, L., Jenkins, J., Ganguly, S., Myneni, R. B., 2011. Canopy spectral invariants, Part 2: Application to classification of forest types from hyperspectral data. Journal of Quantitative Spectroscopy and Radiative Transfer 112 (4), 736–750.

Smolander, S., Stenberg, P., 2005. Simple parameterizations of the radiation budget of uniform broadleaved and coniferous canopies. Remote Sensing of Environment 94 (3), 355–363.

Tang, H., Dubayah, R., 2017. Light-driven growth in amazon evergreen forests explained by seasonal variations of vertical canopy structure. Proceedings of the National Academy of Sciences 114 (10), 2640–2644.

Ter Steege, H., Pitman, N. C., Sabatier, D., Baraloto, C., Salomão, R. P., Guevara, J. E., Phillips, O. L., Castilho, C. V., Magnusson, W. E., Molino, J.-F., et al., 2013. Hyperdominance in the Amazonian tree flora. Science 342 (6156), 1243092.

Tian, H., Melillo, J., Kicklighter, D., McGuire, A., Helfrich Iii, J., Moore Iii, B., Vörösmarty, C., 2000. Climatic and biotic controls on annual carbon storage in Amazonian ecosystems. Global Ecology and Biogeography 9 (4), 315–335.

TRMM, 2011. Tropical Rainfall Measuring Mission Project (2011),TRMM/TMPA 3B43 TRMM and Other Sources Monthly Rainfall Product V7,version 7, Greenbelt, MD:Goddard Space Flight Center Distributed Active Archive Center (GSFC DAAC). Available online: `http://disc.sci.gsfc.nasa.gov/datacollection/TRMM_3B43_V7.html`.

Tucker, C. J., 1979. Red and photographic infrared linear combinations for monitoring vegetation. Remote sensing of Environment 8 (2), 127–150.

van der Tol, C., Berry, J., Campbell, P., Rascher, U., 2014. Models of fluorescence and photosynthesis for interpreting measurements of solar-induced chlorophyll fluorescence. Journal of Geophysical Research: Biogeosciences 119 (12), 2312–2327.

van der Tol, C., Verhoef, W., Timmermans, J., Verhoef, A., Su, Z., 2009. An integrated model of soil-canopy spectral radiances, photosynthesis, fluorescence, temperature and energy balance. Biogeosciences 6 (12), 3109–3129.

Veefkind, J., Aben, I., McMullan, K., Förster, H., De Vries, J., Otter, G., Claas, J., Eskes, H., De Haan, J., Kleipool, Q., et al., 2012. Tropomi on the esa sentinel-5 precursor: A gmes mission for global observations of the atmospheric composition for climate, air quality and ozone layer applications. Remote Sensing of Environment 120, 70–83.

Verrelst, J., Schaepman, M. E., Koetz, B., Kneubühler, M., 2008. Angular sensitivity analysis of vegetation indices derived from CHRIS/PROBA data. Remote Sensing of Environment 112 (5), 2341–2353.

Wang, P., Stammes, P., Pinardi, G., Roozendael, M. v., et al., 2008. FRESCO+: an improved O2 A-band cloud retrieval algorithm for tropospheric trace gas retrievals. Atmospheric Chemistry and Physics 8 (21), 6565–6576.

Widlowski, J.-L., Pinty, B., Clerici, M., Dai, Y., De Kauwe, M., De Ridder, K., Kallel, A., Kobayashi, H., Lavergne, T., Ni-Meister, W., et al., 2011. RAMI4PILPS: An intercomparison of formulations for the partitioning of solar radiation in land surface models. Journal of Geophysical Research: Biogeosciences 116 (G2).

Widlowski, J.-L., Pinty, B., Lopatka, M., Atzberger, C., Buzica, D., Chelle, M., Disney, M., Gastellu-Etchegorry, J.-P., Gerboles, M., Gobron, N., et al., 2013. The fourth radiation transfer model intercomparison (RAMI-IV): Proficiency testing of canopy reflectance models with ISO-13528. Journal of Geophysical Research: Atmospheres 118 (13), 6869–6890.

Wolanin, A., Rozanov, V., Dinter, T., Noël, S., Vountas, M., Burrows, J., Bracher, A., 2015. Global retrieval of marine and terrestrial chlorophyll fluorescence at its red peak using hyperspectral top of atmosphere radiance measurements: Feasibility study and first results. Remote Sensing of Environment 166, 243–261.

Wu, J., Albert, L. P., Lopes, A. P., Restrepo-Coupe, N., Hayek, M., Wiedemann, K. T., Guan, K., Stark, S. C., Christoffersen, B., Prohaska, N., et al., 2016. Leaf development and demography explain photosynthetic seasonality in Amazon evergreen forests. Science 351 (6276), 972–976.

Yang, W., Kobayashi, H., Chen, X., Nishida Nasahra, K., Suzuki, R., Kondoh, A., 2017. Modeling three-dimensional forest structures to drive canopy radiative transfer simulations of bidirectional reflectance factor. International Journal of Digital Earth, 1–20.

Zarco-Tejada, P. J., Miller, J. R., Pedrós, R., Verhoef, W., Berger, M., 2006. Fluormodgui v3. 0: A graphic user interface for the spectral simulation of leaf and canopy chlorophyll fluorescence. Computers & Geosciences 32 (5), 577–591.

A Radiative transfer simulation of SIF and bidirectional reflectance

A three-dimensional Monte Carlo ray-tracing radiative transfer simulation was performed to examine the cause of seasonality in satellite SIF and spectral reflectance in a region within the Amazon Basin. In this study, a spatially explicit three-dimensional model, the Forest Light Environmental Simulator (FLiES), was employed to simulate SIF and spectral bidirectional reflectance seasonality in the wavelength between 650 and 850 nm with a 10 nm interval (Kobayashi and Iwabuchi, 2008; Kobayashi, 2015a, source code: `http://flies.sakura.ne.jp/WP/radiative-transfer-code/`).

FLiES is capable of simulating exact higher order photon scattering under the heterogeneous landscape created by 3D tree objects. When the photons intersected the crowns, we determined the photon path length inside the crowns. The photon path lengths and the scattering directions were determined by random numbers according to a probability distribution function of Lambert–Beers law and a scattering phase function. For the bidirectional reflectance simulation, ray-tracing was initiated from the top of canopy. For the SIF simulation, ray-tracing was initiated on the leaf surface within crowns: The initial positions of photons were determined by the random number. While ray-tracing was performed, bidirectional reflectance and SIF were computed by the local estimation method, which samples the reflectance contributions at every scattering event. The performance and reliability of FLiES for simulating light transmittance through a canopy and bidirectional reflectance factors have been investigated in previous works (Widlowski et al., 2011, 2013).
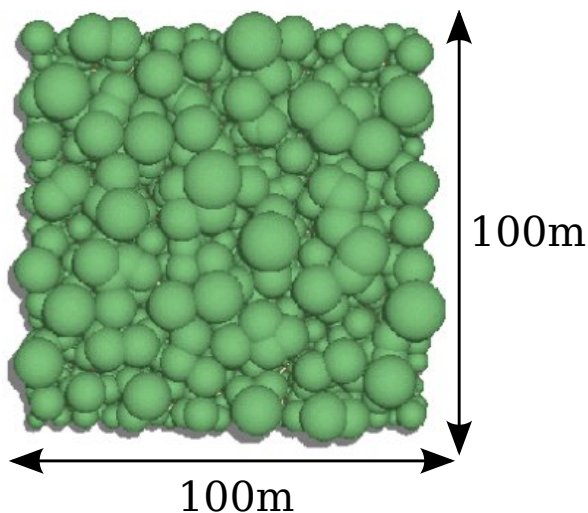

Figure 1: The forest landscape for radiative transfer simulation.

Required inputs for the model include simulated forest landscape data including individual tree position and size. The shape of the tree crown was abstracted as a spheroid and the crown objects were divided into two domains: The outer domains were filled with leaves and inner domains were filled with woody materials. Forest landscape data were constructed based on the empirical forest structure model by Yang et al. (2017). The forest simulation includes a tree density of 2398 trees ha^{-1}, a canopy height of 5 to 50 m following a Weibull distribution and a 99% crown cover. The parameters of the forest structure dynamics model were determined based on the allometric relationships obtained in tropical forests. Figure 1 shows the nadir view of the constructed forest landscape used in the radiative transfer simulation. We adopted the boundary conditions from the sun-sensor geometry of GOME-2 (Sect. 2.7) in combination with monthly averages of the LAI data set for 2014 (Fig. 2 C). Specifically, monthly averages of the solar zenith angle represent a simplified annual cycle of illumination, whereas all discrete viewing zenith angles as well as averages of the two separate regimes of the relative azimuth angle represent the observation geometry (Fig. 2 A & B). The LAI ranges from 4.02 to 5.39 units, incorporating a changing canopy structure (Fig. 2 C). Optical parameters consist of a broadleaf type leaf spectral reflectance and transmittance, woody reflectance (medium reflectivity), and soil reflectance (medium reflectivity) data sets (Fig. 3). These optical data were compiled from the existing literature and publicly available data sets (Kobayashi, 2015b).
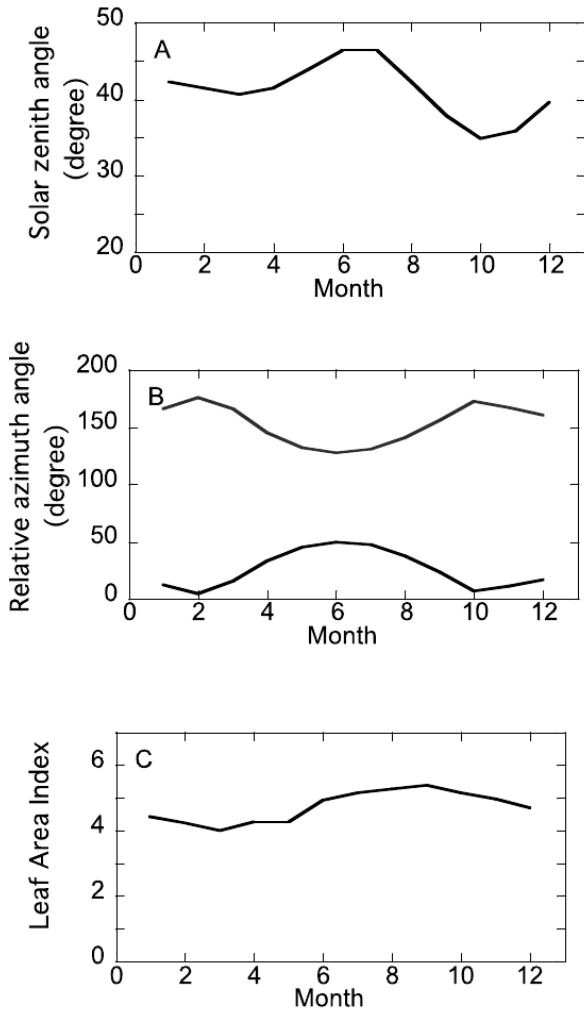
Figure 2: Radiative transfer simulation conditions.
A: Monthly solar zenith angle, B: Relative azimuth angle between sun and GOME-2 sensor, and C: Seasonal landscape scale LAI.

The broadband SIF (integral between 600-800 nm) radiance coming from the leaf surface was derived by the fluorescence yield ϕF, which has been computed based on the fluorescence parameterization framework from van der Tol et al. (2014) in combination with the photosynthesis model by Farquhar et al. (1980) (see red line in Fig. 4). Then, the broadband SIF radiance was converted to spectral SIF radiances at adaxial and abaxial leave sides using the FluorMODleaf (Pedrós et al., 2010) module, which is embedded in the Fluor-MODgui software (Zarco-Tejada et al., 2006). For photosynthesis and broadband SIF simulations, we used a leaf temperature range of 25-36°C, a relative humidity of 50-95%, and a photosynthetically photon flux density (PPFD) ranging from 0-2000 μmol m^{-2} s^{-1}. The maximum carboxylation capacity (Vcmax) was set to 50 μmol m^{-2} s^{-1}, according to the Vcmax of the canopy's top leaves measured by Carswell et al. (2000). We used the Vcmax of the canopy's top layer leaves, because those leaves (mostly sunlit) are expected to contribute the most to canopy scale broadband SIF. In this study, leaf demography variations (seasonal changes in the amount of leaves in each leaf-age class) as observed by Wu et al. (2016) were not incorporated. For the conversion from broadband to spectral SIF with FluorMODleaf, we used a leaf internal structure parameter of 1.5, chlorophyll a+b content of 80 g cm^{-2}, leaf water content of 0.025 cm, dry matter content of 0.01 g cm^{-2}, and a fluorescence quantum efficiency of 0.04 as input parameters. All leaves (sunlit/shaded) in the canopy were assumed to have the same fluorescence yield ϕF, which depends only on the PAR level as shown in Fig. 4. This simplification will likely affect our results, because ϕF is in general different for sunlit and shaded leaves. However, the contribution of shaded leaves to canopy scale SIF in our simulation is rather low (0.32, data are not shown). This means the sunlit contribution dominates, while uncertainties in the SIF yield of shaded leaves represent only a second order effect. Also, a thereby introduced error affects absolute SIF values rather than seasonal patterns, which is our main objective here.

Incident PAR on the leaf surface was computed by the atmospheric module of FLiES. The atmospheric condition is characterized by a tropical temperature profile and a continental aerosol model with an aerosol optical thickness of 0.2 for a cloud-free sky. All of the aforementioned assumptions are likely to deviate from real conditions, which will eventually translate into differences between satellite observations and radiative transfer modeling. However, this strategy enables us to compare a realistic baseline SIF time series under controlled conditions with satellite-based measurements of SIF.
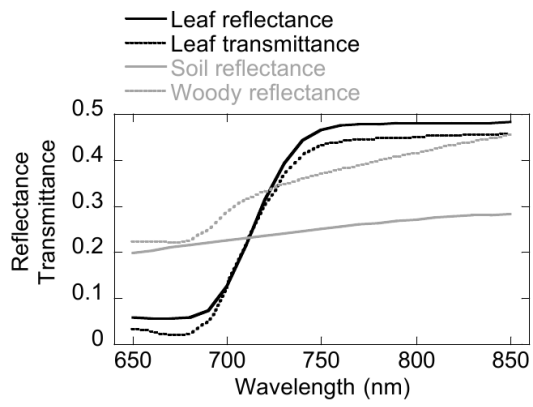
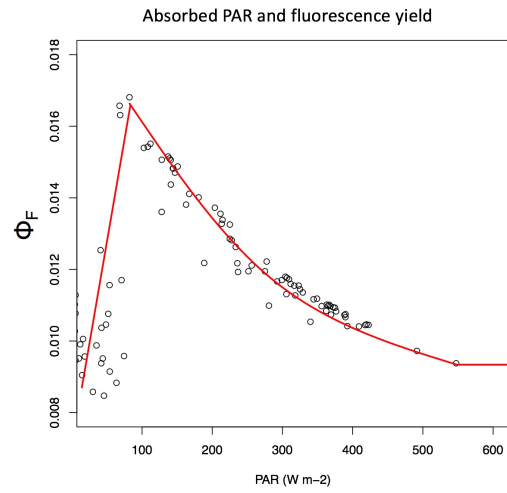Figure 3: Leaf reflectance and transmittance, woody reflectance and soil reflectance.

Figure 4: Leaf level fluorescence yield used in this study.